2012

Investigations of subsonic compressible boundary layer flows using hybrid large eddy simuations

Sara Jo Taylor

Investigations of Subsonic Compressible Boundary Layer Flows using Hybrid Large Eddy Simulations

by

Sara Jo Taylor

A THESIS

Submitted in partial fulfillment of the requirement
for
the degree of Master of Science in Engineering
in
The Department of Chemical and Material Engineering
to
The School of Graduate Studies
of
The University of Alabama in Huntsville

HUNTSVILLE, ALABAMA

2012

In presenting this thesis in partial fulfillment of the requirements for a master's degree from The University of Alabama in Huntsville, I agree that the Library of this University shall make it freely available for inspection. I further agree that permission for extensive copying for scholarly purposes may be granted by my advisor or, in his absence, by the Chair of the Department or the Dean of the School of Graduate Studies. It is also understood that due recognition shall be given to me and to The University of Alabama in Huntsville in any scholarly use which may be made of any material in this thesis.

Sara Jo Taylor 12/2/12

(student signature) (date)

THESIS APPROVAL FORM

Submitted by Sara Jo Taylor in partial fulfillment of the requirements for the degree of Master of Science in Engineering and accepted on behalf of the Faculty of the School of Graduate Studies by the thesis committee.

We, the undersigned members of the Graduate Faculty of The University of Alabama in Huntsville, certify that we have advised and/or supervised the candidate on the work described in this thesis. We further certify that we have reviewed the thesis manuscript and approve it in partial fulfillment of the requirements for the degree of Master of Science in Engineering.

8/9/2012 Committee Chair
(Date)

Department Chair

College Dean

Graduate Dean

ABSTRACT

The School of Graduate Studies
The University of Alabama in Huntsville

Degree Master of Science in Engineering .
College/Dept. Engineering/Chemical and Materials Engineering .
Name of Candidate Sara Jo Taylor .
Title Investigations of Subsonic Compressible Boundary Layer Flows using Hybrid Large Eddy Simulations .

The objective of this thesis is to investigate the spatially developing turbulent compressible boundary layer on a flat plate using the Spalart-Allmaras Detached Eddy Simulation (SA-DES) model [22] and the Nichols-Nelson hybrid Reynolds-Averaged Navier-Stokes/Large Eddy Simulation (RANS/LES) model [13] which have been implemented into the Wind-US 3.0 computational fluid dynamics code [30]; both of the hybrid approaches involve RANS modeling in the near-wall region and LES treatment in the outer region. Generation of unsteady turbulent inflow data is achieved via the prescribed energy spectrum method. The studies illustrated dependence on Reynolds number based on momentum thickness, Re_θ, ranging from 3018 to 19430, and dependence on Mach number, $M = 0.5$ and $M = 0.9$. The SA-DES model predicted mean flow profiles to a satisfactory degree, and the Nichols-Nelson hybrid RANS/LES model adequately predicted density field fluctuations; the aero-thermal effects captured by the Nichols-Nelson model can be useful for near-field aero optics applications.

Abstract Approval: Committee Chair _____

Department Chair _____

Graduate Dean Rhonda Kay Baede 12/11/12

ACKNOWLEDGMENTS

I would like to express deep thanks to my advisor, Dr. C. P. Chen, whom I greatly admire and respect, for his guidance and intellectual insight throughout my graduate and undergraduate studies. I would also like to thank the other members of my thesis committee, Dr. Banish and Dr. Ramachandran for donating their time and efforts on my behalf. I am also appreciative of my colleagues Omid Samimi, James Keane, and John Price, as they have all been very kind and helpful. A special thanks is extended to my very best friends Drew Bolling and Lacey Miller, my girlfriend Morgan Brooks, my sister Emme Taylor, and my parents Keith and Jenny Taylor for undying support and genuine love and encouragement throughout my studies. My grandparents, Robert and Lil Wood, have been the sweetest roommates whose roles in my daily life as a graduate student has been invaluable. Lastly, I am grateful for financial support provided by the Chemical and Materials Engineering department.

TABLE OF CONTENTS

LIST OF FIGURES

LIST OF TABLES

LIST OF ACRONYMS

Acronym	Definition
RANS	Reynolds-Averaged Navier-Stokes
LES	Large Eddy Simulation
MTF	Modulation Transfer Function
HRLES	Hybrid RANS/LES
DNS	Direct Numerical Simulation
N-S	Navier-Stokes
SST	Sheer Stress Transport
CPU	Central Processing Unit
SGS	Sub-grid Scale
LES-NWM	Large Eddy Simulation with Near-Wall Modeling
SA-DES	Spalart-Allmaras Detached Eddy Simulation
DDES	Delayed Detached Eddy Simulation
SST-DES	Shear Stress Transport-Detached Eddy Simulation
ZDES	Zonal Detached Eddy Simulation
PDF	Probability Density Function
OPD	Optical Path Difference
HLLC	Harten-Lax-van Leer for Contact

LIST OF SYMBOLS

Symbol	Definition
x, y, z	Stream-wise, wall-normal and span-wise coordinates for flow
x', y', z'	Optical coordinates
z'	Optical propagation direction
Re	Reynolds number
θ	Momentum thickness
Re_θ	Reynolds number based on momentum thickness
k	turbulent kinetic energy
ε	turbulent kinetic energy dissipation rate
ω	turbulent kinetic energy dissipation
ν	kinematic viscosity
ρ	fluid density
u	fluid velocity
P	pressure
δ_{ij}	Kronecker delta
τ_{ij}	viscous shear stress
e	specific internal energy
h	specific enthalpy
q	heat flux
R	ideal gas constant
T	temperature
μ	dynamic viscosity

C	Sutherland's law constant
C_v	heat capacity at constant volume
k_c	thermal conductivity
ϕ	generic dependent variable
μ_L	laminar viscosity
Pr	Prandtl number
μ_T	dynamic turbulent viscosity
$\tilde{\nu}$	Spalart-Allmaras transport equation quantity
Ω	magnitude of the local mean flow vorticity
τ_{ij}^{sgs}	subgrid stress
C_s	Smagorinsky constant
L_g	grid length scale
S_{ij}	filtered strain rate tensor
k_{sgs}	subgrid turbulent kinetic energy
C_k	K-equation model constant
d	distance to wall
C_{DES}	Spalart-Allmaras DES constant
L_T	turbulent length scale
$\nu_{T_{RANS}}$	RANS-modeled turbulent viscosity
k_{LES}	Nichols-Nelson subgrid turbulent kinetic energy
M	Mach number

U_∞	freestream velocity
δ_0	inlet boundary layer thickness
$Re_{\delta 0}$	Reynolds number based on boundary layer thickness
w_i	interpolation weight
r, s	coordinates of the interpolation point
d	interpolated value
d_i	data value at point P_i
β	elevation angle
δ	local boundary layer thickness

Superscript

+	Wall unit normalization

Subscript

rms	Root mean square
0	initial condition
∞	free stream condition

CHAPTER ONE

Introduction

The spatially developing boundary layer in turbulent flow is a fundamental fluid flow problem. It is often used as a benchmark case, as the self-similar statistical profiles associated with flow over a flat plate can be readily compared with those in literature. Two challenges of simulating the spatially developing turbulent boundary layer are the requirement of prescribing time-dependent turbulent inflow conditions at the inflow boundary and generating a domain long enough in the streamwise direction to allow the boundary layer to become fully developed. The cases presented herein are simulated with numerical solutions of the compressible Navier-Stokes equations because the Mach numbers, $M = 0.5$ and $M = 0.9$, are above the threshold that can be accurately treated as incompressible but shy of the supersonic region wherein the effects of phenomena such as shock waves need to be considered.

Spatially developing boundary layers have been studied previously [26, 27, 28, 29] using Large Eddy Simulation methodologies. In LES the outer layer resolution scales as $Re^{0.4}$, but the required number of grid points in the near-wall region scales as $Re^{1.8}$ [15], thus, due to stringent grid size requirements of resolving the near-wall turbulence, these studies were limited to lower Reynolds number regimes. In this study, a wall-modeled LES utilizing a hybrid RANS/LES (Reynolds-Averaged Navier-Stokes/Large

Eddy Simulation) turbulence modeling approach is used for three cases (each case is run with two different hybrid models): one with $Re_\theta = 2900$, comparable to those studied previously [3, 26, 27, 29], and two with a range $Re_\theta = 9000$ to 19000, higher than any of the Reynolds numbers referenced herein.

The objective of this paper is to investigate aero thermal aspects of a spatially developing subsonic boundary layer. Two hybrid Large Eddy Simulation methods were used, the Spalart-Allmaras Detached Eddy Simulation model [22] and the Nichols-Nelson hybrid RANS/LES model [13]. Fluid behavior along view vectors within a flow-field generated with Wind-US 3.0 [30] was analyzed, giving special attention to the density fluctuations. Trends shown by analysis of view vectors elevated to different angels demonstrates that hybrid RANS/LES methods are capable of capturing the anisotropic vortical structures and provides information that can be useful for aero optical calculations.

1.1 Numerical Simulation of Turbulence

Turbulent flow is characterized by significant variation and irregularity of flow quantities over time and three-dimensional space, as well as enhanced mass, momentum, and energy transfer induced by the vigorous mixing that is inherent to turbulence. The characteristic size of turbulent motion spans across length scales that range from the characteristic width of the flow to the smallest eddy; additionally, associated with each eddy is a characteristic velocity, thus turbulent flow covers a range of time scales. The energy contained within the fluid in motion is introduced in the largest scales and is transferred to smaller and smaller scales until the cascade is complete with viscous

dissipation. The broad range of time and length scales to be simultaneously captured attributes to the difficulty in simulating turbulence.

The application for which turbulent flow is being simulated determines the level of fidelity required of the model. The following methods of simulation are all based on the numerical solution of the Navier-Stokes (N-S) equations but differ in complexity, accuracy, and computational cost: (1) Direct Numerical Simulation, (2) Large Eddy Simulation (LES), (3) Reynolds-Averaged Navier-Stokes (RANS) modeling, and (4) Hybrid RANS/LES (HRLES) modeling.

1.1.1 Direct Numerical Simulation (DNS)

DNS is the most rigorous of the methods, numerically solving the full, unmodified Navier-Stokes equations, avoiding modeling assumptions and resolving all of the scales of motion. With such fidelity comes a great computational cost. A grid that can accommodate resolution of the smallest eddies as well as capture the large ones requires a domain consisting of a tremendous number grid points, proportional to $Re^{9/4}$[17], is the main contributor to cost; also, with the only errors introduced being from numerical approximation, high order numerical schemes, which are appropriate only for simple geometries, are routine within DNS [1]. Limited to low Reynolds number flow over simple geometries, DNS is primarily used as research tool, rather than as a method of simulating an applicable engineering problems; DNS has provided insight into turbulent physics not producible by laboratory experiments and served as a method of validation of other simulation techniques [19, 11].

1.1.2 Reynolds-Averaged Navier-Stokes (RANS)

While DNS solves the Navier-Stokes equations to determine the instantaneous velocity field for one realization of the flow, RANS approaches determine the mean velocity field over a given time period [17]. The Navier-Stokes equations are decomposed and time-averaged to obtain the RANS equations, which contain a term extraneous to the unmodified N-S equations, Reynolds stress. This additional unknown renders the RANS equations an unclosed set; closure is sought by determining these Reynolds stresses via a turbulent viscosity model or modeled Reynolds-stress transport equations.

Turbulent viscosity models relate the Reynolds stress to the mean rate of strain by the modeled turbulent viscosity based on Boussinesq's turbulent-viscosity hypothesis [17]; they are classified as algebraic, one-equation, or two-equation models. Algebraic RANS models, such as the uniform turbulent viscosity and the mixing length models, employ an empirical formulation for the turbulent viscosity. In the turbulent-kinetic-energy model, a one-equation model, the eddy viscosity is calculated based on the specified mixing length and kinetic energy, which is estimated by solving a model transport equation. Two-equation models consist of the same model transport equation for kinetic energy (k) as the one-equation model mentioned above, as well as a model transport equation for the turbulent kinetic energy dissipation (ε or ω); the turbulent viscosity is calculated from these two quantities via the k-ε model or k-ω model, so a length scale need not be specified. Menter's k-ω Shear Stress transport model (SST) is an example of a blend of k-ε and k-ω models [10]. The Spalart-Allmaras model falls between the one- and two-equation models, solving a single model transport equation,

based on the laminar viscosity, the mean vorticity, and the distance to the nearest wall, for the turbulent viscosity.

The turbulent-viscosity hypothesis is not needed in Reynolds stress models as model transport equations are solved for the individual Reynolds stresses and for the turbulent kinetic energy dissipation (ε or ω) [17]. The principle quantity to be modeled is the pressure-rate-of-strain tensor, effectively governed by the Poisson equation. While use of a Reynolds stress model provides a higher level of description than turbulent-viscosity models, the Central Processing Unit (CPU) time is double that of a two-equation turbulent-viscosity model.

Computing only the mean flow field takes considerably less computational resources than determining the instantaneous flow field. The cost reduction is the main appeal of RANS, however the drawback is its inability to provide instantaneous information for unsteady flow, necessary in aero-acoustics and aero-optics. Another advantage of RANS is that it lends itself to complex geometries by use of lower order numerical schemes. RANS is an appropriate method for attached flows or flow with large-scale or low-frequency unsteadiness, and can be implemented without limitation by Reynolds number or flow geometry.

1.1.3 Large Eddy Simulation (LES)

As in DNS, LES determines the instantaneous velocity field for one realization of the flow, however, in LES the full Navier-Stokes equations are spatially filtered, and only the length scales larger than the filter width are resolved; these larger length scales are associated with the large, energy carrying structures. Those length scales eliminated by the filter must be modeled to achieve closure; that is, the energy must be effectively

removed from the resolved scales to complete the energy cascade [16]. Kolmogorov's first similarity hypothesis provides justification for modeling the effect of the smallest turbulent scales, rather than computing them exactly: *In every turbulent flow at sufficiently high Reynolds number, the statistics of the small-scale motions* (those below the energy containing range) *have a universal form that is uniquely determined by ν* (kinematic viscosity*) and ε* (dissipation rate) [17]. Introducing a model for the smallest dissipative motions, alleviates the computational effort required by DNS to resolve them, yet retains the explicit computation of the large scale unsteady motions of interest in unsteady aerodynamic applications.

The filter operation and the subgrid-scale model (SGS) are the two components of LES to be chosen by the user. Some commonly used filter functions are the sharp Fourier cutoff filter, the Gaussian filter, and the tophat filter [16]; the filter width should correspond to the smallest mesh size to ensure that the scales above the filter width are directly resolved [1]. Most subgrid-scale models are eddy viscosity models that relate the subgrid-scale stresses to the large-scale strain-rate [16]; in the commonly used Smagorinsky model, the assumption that the small scales are in equilibrium—instantaneously dissipating the energy received from the large scales, leads to an algebraic model for the eddy viscosity [16].

Resolution of the near-wall region, of importance in wall-bounded flows, becomes a source of computational cost in LES, particularly at high Reynolds numbers as the size of the smallest eddy decreases as the Reynolds number increases; while the outer layer resolution scales as $Re^{0.4}$, the required number of grid points in the near-wall region scales as $Re^{1.8}$ [15]. An alternative, Large Eddy Simulation with near-wall

modeling (LES-NWM), was introduced to overcome the Reynolds number limitation making this variation of LES suitable for practical engineering use. If direct modeling of the residual stress tensor is incorporated into the LES-NWM method, the approach is still considered a variation of LES because the instantaneous fluctuating velocity and temperature field are modeled; however, if the near-wall region is simulated with RANS, in which only the mean field is modeled, the method is considered hybrid RANS/LES methods [15].

1.1.4 Hybrid RANS/LES

Hybrid RANS/LES methods incorporate a modified RANS model in the near-wall region; a transition to LES away from the wall allows for the large unsteady turbulent structures to be captured. This method lends itself to compute high Reynolds number flows more efficiently than traditional LES. Nichols and Nelson [14] describe two possibilities for developing hybrid models from existing RANS models.

The first method is to modify the production or dissipation source terms in the turbulence model so that the turbulence quantities normally transported by the RANS turbulent model would be created or destroyed based on local grid resolution; examples of this type of hybrid RANS/LES approach are the Spalart-Allmaras Detached Eddy Simulation (SA-DES) [22], Delayed Detached Eddy Simulation (DDES) [22], Shear Stress Transport-Detached Eddy Simulation (SST-DES) [23] and Zonal Detached Eddy Simulation (ZDES) [4].

The second approach is to solve the existing RANS turbulence model and then filter the results to determine the level of eddy viscosity that will be used in the solution of the Navier-Stokes equations; the Nichols-Nelson hybrid RANS/LES method is an

example of this approach. Nichols and Nelson designate their model as a multiscale model implemented in conjunction with the SST two-equation turbulence model [14].

A representative of each approach has been applied to the flat plate case presented in this thesis: (1) SA-DES and (2) Nichols-Nelson hybrid RANS/LES:

(1) SA-DES has been applied with good results to various geometries over a range of Mach numbers [14, 21]; however, the transition from RANS to LES is exclusively a function of local grid spacing, so the grid must be generated in a manner that coincides with the model requirements, else, as Spalart remarks in [22], grid-induced separation can result.

(2) The Nichols-Nelson hybrid RANS/LES transitions from RANS to LES as a function of the ratio of the local turbulent length scale predicted by the RANS model to the local grid spacing, [14], requiring less user input than SA-DES.

1.2 Inflow Boundary Conditions

Unsteady simulations of flow over a flat plate require generation of unsteady turbulent inflow data since this geometry lacks a protrusion to prompt the transition into turbulent flow. The mean quantities can be inferred from experiments and other well established simulations; however the fluctuation must be generated for each case to simulate the irregularity of turbulence. The method of inflow data generation effects computational cost by requiring an auxiliary simulation from which the inflow data is extracted or by requiring a much longer computational domain so the flow can recover from an imposed unrealistic condition [20].

(1) Precursor Simulation

The precursor simulation method involves extracting a plane from an auxiliary simulation, of equal fidelity as the main simulation (DNS or LES), and using that data as the inlet conditions for the main simulation [6]. This increases computational effort by requiring an additional domain that can accommodate the auxiliary simulation, whose results must then be stored. The advantage of the precursor technique to simply using a long calculation domain is that it allows for splitting of the domain; the recovery region is relatively short in the main simulation domain. An additional step can be taken to hasten development of the precursor simulation; the extraction-rescaling technique involves extracting the velocity field at a downstream station on the auxiliary domain, rescaling and re-introducing it at the inlet of the auxiliary simulation [9]. Said method is employed by Tromuer in [26].

(2) Prescribed Probability Density Function

An approach based on a prescribed Probability Density Function (PDF) was used by [2]. This method also requires an auxiliary simulation, however instead of the computationally expensive DNS or LES auxiliary simulations referred to in (1), a given flow field is generated by a RANS simulation. A joint normal distribution function is defined based on first- and second-order velocity correlations and random samples are taken from the distribution function, resulting in a turbulent inflow plane that preserves the these velocity correlations

(3) Random Fluctuations with Prescribed Mean Velocity Profile

The simplest method of generating inflow turbulence is to superimpose random fluctuations on a prescribed mean velocity profile at the inlet of the simulation domain.

While constraints can be imposed to satisfy desired some statistics, higher order correlations are incorrect, thus the flow lacks realistic turbulent structure [9]. The computational savings of only running one simulation, as opposed to running both an auxiliary and a main simulation, are generally offset by the length of the recovery region needed to develop organized turbulent motion.

(4) Random Fluctuation with Prescribed Energy Spectrum

The first step in this process is to calculate a pseudorandom divergence-free isotropic velocity field that conforms to a prescribed energy spectrum; this velocity field is generated in a box at the inlet of the simulation. Given the assumed energy spectrum and a sufficiently low peak wave number, this level of resolution is sufficient to capture the majority of the energy-containing wave-numbers [8]. This approach is used by [3].

(5) Emulating Experimental Conditions

In experimental studies of flow over a flat plate, turbulence is often geometrically tripped at some point in the upstream (with a wire or backward facing step), and the region of interest is taken far enough downstream to justify the geometry as a flat plat, despite the introduced protrusion. Another method is to create a mixing layer by having two regions of fluid flow, the upper, free-stream region at a given Mach number and a region that extends to the wall at a lower Mach number, flow in parallel; the region of interest is taken far enough downstream that the two layer can be considered sufficiently mixed. In addition to creating turbulence, these methods also enhance boundary layer growth, which can dramatically reduce the streamwise length of the computational domain. A geometric trip creates a recirculation zone after which the boundary layer starts and continues to grow. The mixing layer theory involves boundary layer development that

spurs from the point of contact between the mixing layer and original slowly developing boundary layer.

1.3 Objective

The objective of this paper is to investigate aero thermal aspects of a spatially developing subsonic boundary layer employing two hybrid RANS/LES models within the Wind-US 3.0 CFD code. Analysis of the aero thermal behavior of the fluid along view vectors elevated to different angels demonstrates that hybrid RANS/LES methods are capable of capturing the anisotropic behavior and providing information that is valuable for aero optical calculations, such as those of [26, 27, 28, 29].

The simulation methods presented are SA-DES and Nichols-Nelson hybrid RANS/LES; turbulence and boundary layer growth are achieved via a combination of artificial turbulence injection and mixing layer development described in (4) and (5) in section 1.2, respectively, whereby a velocity field with random fluctuations which adhere to a prescribed energy spectrum is injected into the lower Mach number flow region of the two-stream flow.

1.4 Outline

This thesis is organized into five chapters. The first chapter provides information on the various options for turbulence simulation. Chapter Two presents the governing equations for the simulation techniques of interest. In Chapter Three, the computational set-up is detailed for each case studied, and results and discussion of these cases is presented in Chapter Four. Chapter Five consists of concluding remarks and recommendations.

CHAPTER TWO

Governing Equations

2.1 The equations of fluid motion

The Navier-Stokes equations govern the flow of Newtonian fluids; the equation set, comprised of time-dependent equations for the conservation of mass, momentum, and energy, is reviewed in tensor notation below [1]:

$$\frac{\partial \rho}{\partial t} + \frac{\partial \rho u_j}{\partial x_j} = 0, \tag{2.1}$$

$$\frac{\partial \rho u_i}{\partial t} + \frac{\partial \rho u_i u_j}{\partial x_j} = \frac{\partial}{\partial x_j}\left(-P\delta_{ij} + \tau_{ij}\right), \tag{2.2}$$

$$\frac{\partial}{\partial t}\left[\rho\left(e + \frac{u_i u_i}{2}\right)\right] + \frac{\partial}{\partial x_j}\left[\rho u_j\left(h + \frac{u_i u_i}{2}\right)\right] = \frac{\partial}{\partial x_j}\left(u_i \tau_{ij} - q_j\right), \tag{2.3}$$

where ρ is the fluid density, u is the fluid velocity, P is pressure, δ_{ij} is the Kronecker delta, which equals 1 if $i = j$ and 0 if i ≠ j, τ_{ij} is the viscous shear stress, e is the specific internal energy, h is the specific enthalpy, and q is heat flux.

Equations the last four quantities are presented below.

The perfect gas law is applied, as local thermodynamic equilibrium is assumed everywhere in the flow:

$$P = \rho RT \ , \tag{2.4}$$

where R is the ideal gas constant and T is temperature. The viscous stress tensor is given by

$$\tau_{ij} = \mu\left(\frac{\partial u_i}{\partial x_j} + \frac{\partial u_j}{\partial x_i} - \frac{2}{3}\frac{\partial u_k}{\partial x_k}\delta_{ij}\right), \tag{2.5}$$

where μ is the dynamic viscosity of the fluid which is assumed to vary only with temperature according to Sutherland's law:

$$\mu = \mu_0 \frac{T_0 + C}{T + C}\left(\frac{T}{T_0}\right)^{\frac{3}{2}}, \tag{2.6}$$

where C is a constant associated with the particular fluid. The specific internal energy, e is calculated by:

$$e = C_v T \tag{2.7}$$

C_v is heat capacity at constant volume. The specific enthalpy also includes the internal energy as:

$$\rho h = \rho e + P \ . \tag{2.8}$$

The heat flux is

$$q_j = -k_c \frac{\partial T}{\partial x_j}, \tag{2.9}$$

where k_c is the thermal conductivity.

2.2 RANS Simulation

The formulation of the RANS approach, including the formulation of two closure models, is presented in this section.

2.2.1 RANS Equations

The first step in obtaining the Reynolds-Averaged Navier-Stokes equations is Reynolds decomposition, by which each dependent turbulent variable, generically represented below as ϕ, is decomposed into its mean, $\overline{\phi}$, and the fluctuation, ϕ', as follows:

$$\phi \equiv \overline{\phi} + \phi'. \tag{2.10}$$

The mean quantity, indicated by an overbar, is the statistical ensemble average of the instantaneous quantity:

$$\overline{\phi}(X,t) \equiv \frac{1}{N}\sum_{n=1}^{N} \phi^{(n)}(X,t); \tag{2.11}$$

that is, $\phi^{(n)}$ is the value of the flow quantity at instant *n*, and *N* is the number of instances, or realizations, over which the average is taken.

Decomposing and averaging the Navier-Stokes equations yields the RANS equations:

$$\frac{\partial}{\partial t}\overline{\rho} + \frac{\partial}{\partial x_j}\overline{\rho}\overline{u}_j = 0\,, \tag{2.12}$$

$$\frac{\partial}{\partial t}\overline{\rho}\overline{u}_i + \frac{\partial}{\partial x_j}\overline{\rho}\overline{u}_i\overline{u}_j = \frac{\partial}{\partial x_j}\left[-\overline{P}\delta_{ij} + \left(\tau_{ij}^L + \tau_{ij}^T\right)\right], \tag{2.13}$$

$$\frac{\partial}{\partial t}\left[\overline{\rho}\left(\overline{e} + \frac{\overline{u}_i\overline{u}_i}{2} + k\right)\right] + \frac{\partial}{\partial x_j}\left[\overline{\rho}\overline{u}_j\left(\overline{h} + \frac{\overline{u}_i\overline{u}_i}{2} + k\right)\right] = \frac{\partial}{\partial x_j}\left[\overline{u}_i\left(\tau_{ij}^L + \tau_{ij}^T\right) - (q_j^L + q_j^T)\right]. \tag{2.14}$$

All terms have been previously defined, or can be found by applying Reynolds decomposition (in the case of $\overline{\rho}$, $\overline{P}$, $\overline{e}$, and $\overline{h}$), except the kinetic energy, *k*, and those with the *L* (laminar) or *T* (turbulent) superscript, which are defined below; those with a *T* superscript are the unresolved terms that result from Reynolds decomposition and averaging.

The laminar stress tensor and heat flux are given by

$$\tau_{ij}^L = \mu_L\left(\frac{\partial}{\partial x_j}\overline{u}_i + \frac{\partial}{\partial x_i}\overline{u}_j - \frac{2}{3}\frac{\partial}{\partial x_k}\overline{u}_k\delta_{ij}\right), \tag{2.15}$$

$$q_j^L = -\frac{\mu_L}{\mathrm{Pr}}\frac{\partial}{\partial x_j}\overline{h}\,, \tag{2.16}$$

where μ_L is the laminar viscosity as defined by Sutherland's Law, and *Pr* is the Prandtl number:

$$\mathrm{Pr} = \frac{C_p\mu_L}{k_c} \tag{2.17}$$

The turbulent stress, heat flux, and kinetic energy are given as

$$\tau_{ij}^T = -\overline{u_i'u_j'} \tag{2.18}$$

$$q_j^T = \overline{\rho}\overline{u_j'h'} \tag{2.19}$$

$$\overline{\rho}k = \frac{\overline{\rho}\overline{u_i'u_i'}}{2} \tag{2.20}$$

Closure to this set of equations is sought by attaining the Reynolds stress with a model. Of the methods mentioned in 1.1.2, two turbulent viscosity models, the Spalart-Allmaras model and Menter's k-ω Shear Stress transport model (SST), will be discussed in the following sections as these two methods are employed in the hybrid RANS/LES simulations studied. These two models aim to determine the turbulent viscosity, μ_T, to the solve for the Reynolds stress via the turbulent viscosity hypothesis equation below:

$$-\rho\overline{u_i'u_j'} + \frac{2}{3}\rho k\delta_{ij} = \mu_T\left(\frac{\partial}{\partial x_j}\overline{u}_i + \frac{\partial}{\partial x_i}\overline{u}_j\right), \tag{2.21}$$

2.2.2 Spalart-Allmaras model

The one-equation model proposed by Spalart and Allmaras is presented below. This equation is solved for the quantity, $\tilde{\nu}$, that is subsequently used to calculate the turbulent viscosity.

$$\frac{\partial}{\partial t}\tilde{\nu} + u_j\frac{\partial}{\partial x_j}\tilde{\nu} = c_{b1}\left(1 - f_{t2}\right)\tilde{S}\tilde{\nu} - \left(c_{\omega 1}f_\omega - \frac{c_{b1}}{k^2}f_{t2}\right)\left(\frac{\tilde{\nu}}{d}\right)^2 + \frac{1}{\sigma}\left[\frac{\partial}{\partial x_j}\left(\nu + \tilde{\nu}\right)\frac{\partial}{\partial x_j}\tilde{\nu} + c_{b2}\frac{\partial}{\partial x_j}\tilde{\nu}\frac{\partial}{\partial x_j}\tilde{\nu}\right] \tag{2.23}$$

$\tilde{\nu}$ is a term introduced in this model that is related to the turbulent viscosity by a weighting function, f_{v1}

$$\mu_T = \overline{\rho}\tilde{\nu}f_{v1}. \tag{2.24}$$

The weighting function, f_{v1} , is such that $\tilde{\nu}$ is equal to the kinematic turbulent viscosity, $\nu_T \left(=\frac{\mu_T}{\rho}\right)$,except in the viscous range, where it behaves linearly to the wall. In the above equation $\left(c_{\omega 1} f_\omega - \frac{c_{b1}}{k^2} f_{t2}\right)\left(\frac{\tilde{\nu}}{d}\right)^2$ is the modified destruction term based on the distance to the wall *d*, mentioned in section 1.1.4.

Details on the weighting functions, constant values, and expansion of other terms can be found in [21].

2.2.3 Menter's SST model

As mentioned in 1.1.2, Menter's shear stress model is a blend of k-ε and $k-\omega$ models, taking advantage of the $k-\omega$ model's effectiveness near the wall and exploiting the stability of the k-ε model in the outer region. The following equation set leads to determination of k and ω, which yields the turbulent viscosity via equation 2.27. The k-equation is

$$\frac{D}{Dt}(\bar{\rho}k) = \tau_{ij}\frac{\partial u_i}{\partial x_j} - \beta^*\bar{\rho}\omega k + \frac{\partial}{\partial x_j}\left[(\mu + \sigma_k \mu_T)\frac{\partial k}{\partial x_j}\right], \tag{2.25}$$

and the ω-equation is

$$\frac{D}{Dt}(\bar{\rho}\omega) = \frac{\gamma\bar{\rho}}{\mu_T}\tau_{ij}\frac{\partial u_i}{\partial x_j} - \beta\bar{\rho}\omega^2 + \frac{\partial}{\partial x_j}\left[(\mu + \sigma_\omega \mu_T)\frac{\partial \omega}{\partial x_j}\right] + (1 - F_1)\bar{\rho}\frac{2\sigma_{\omega 2}}{\omega}\frac{\partial k}{\partial x_j}\frac{\partial \omega}{\partial x_j}. \tag{2.26}$$

F_1 is a blending function that goes from one near the wall to zero away from the wall.

The turbulent viscosity is defined as

$$\mu_T = \frac{\rho a_1 k}{\max(a_1 \omega, \Omega F_2)}, \tag{2.27}$$

where Ω is the magnitude of the local mean flow vorticity, and F_2 is a blending function that is equal to one inside boundary layers and goes to zero for free shear layers. Details on the blending functions, constant values, and expansion of other terms can be found in [1,10]. In the interest of high-fidelity aero-optic results along elevated lines of sight, a more sophisticated interpolation scheme is suggested.

2.3 Large Eddy Simulation

By redefining the decomposition and averaging process, the equations for large eddy simulation can be presented as those for the Reynolds-averaged Navier Stokes equations in section 2.2.1 [18]; each dependent turbulent variable, ϕ, is decomposed into its spatially filtered part, $\overline{\phi}$, and subgrid part, ϕ', as follows:

$$\phi \equiv \overline{\phi} + \phi'. \tag{2.28}$$

here, the overbar that represents the Reynolds average in the RANS equations instead represents the filtering function:

$$\overline{\phi}(x) = \int_{-\infty}^{\infty} G(r, \Delta)\phi(x - r)dr, \tag{2.29}$$

where the function $G(r, \Delta)$ can be specified as the sharp Fourier cutoff filter, the Gaussian filter, and the tophat filter as mentioned in section 1.1.3. The prime notation in the LES equation set represents the part of the quantity that is deemed too small by the filter, thus the Reynolds stress terms in the RANS equations are termed subgrid stress in

LES; as with the Reynolds stresses, the subgrid stresses are modeled to achieve closure of the equation set. Most subgrid modeling techniques used with LES are turbulent viscosity models, as is the case for RANS modeling. One such model is the constant coefficient Smagorinsky model, which calculates the subgrid stress, τ_{ij}^{sgs}, by:

$$\tau_{ij}^{sgs} = -\nu_T \left(\frac{\partial}{\partial x_j} \overline{u}_i + \frac{\partial}{\partial x_i} \overline{u}_j \right) - \frac{2}{3} k \delta_{ij}, \tag{2.30}$$

where the kinematic turbulent viscosity is modeled as:

$$\nu_T = \left(C_s L_G \right)^2 \sqrt{2 S_{ij} S_{ij}}, \tag{2.31}$$

where C_s is the Smagorinsky constant, L_G is proportional to the local grid spacing and S_{ij} is the filtered strain rate tensor:

$$S_{ij} = \frac{1}{2} \left(\frac{\partial \overline{u}_i}{\partial x_j} - \frac{\partial \overline{u}_j}{\partial x_i} \right). \tag{2.32}$$

Another, more physically descriptive model is the k-equation model, in which the turbulent kinematic viscosity is formed from the subgrid turbulent kinetic energy, k_{sgs}, and a grid length scale, L_G, as:

$$\nu_T = C_k L_G \sqrt{k_{sgs}} \tag{2.33}$$

where C_k is a model constant.

In the present study, a hybrid RANS/LES approach is employed, seeking closure by modeling the near-wall region with RANS and transitioning into one of the LES subgrid models mentioned above.

2.4 Hybrid RANS/LES

The formulation for the two methods of hybrid RANS/LES models, Spalart-Allmaras DES and Nichols-Nelson hybrid RANS/LES are presented in this section.

2.4.1 Spalart-Allmaras DES

In the Spalart-Allmaras DES approach, the destruction term is modified to control the turbulent viscosity based on grid spacing by replacing the distance to the wall *d* by:

$$\tilde{d} = \min\left(d, C_{DES} L_G\right). \tag{2.34}$$

The grid length scale, based on local grid lengths Δx, Δy, and Δz is defined as

$$L_G = \max\left(\Delta x, \Delta y, \Delta z\right), \tag{2.35}$$

and $C_{DES} = 0.65$. With this modification, the DES model reduces to the standard Spalart-Allmaras RANS model near the viscous wall, where the grid is refined and has a large aspect ratio, but behaves like a Smagorinsky LES turbulence model when L_g is less than the distance from the wall.

2.4.2 Nichols-Nelson hybrid RANS/LES

The Nichols-Nelson approach attempts to reduce grid dependence by employing a more complex formulation that incorporates the turbulent length scale, L_T, into the switching function to facilitate a smooth transition from RANS turbulence model behavior to LES subgrid model behavior as the computational grid resolution changes. Being function of both the local grid spacing (L_G) and the local turbulent length scale (L_T) rather than simply being a function of grid spacing alone, as is the case for DES, allows the filter function to detect whether the grid can resolve the local turbulent scales before transitioning to the LES mode. Nichols and Nelson introduce their approach as a

derivative of the multi-scale turbulence model of [7] which is a two-equation k-ε model that differentiates between large-scale turbulence (subscript p) and the smaller, more dissipative turbulent scales (subscript t), and thus is comprised of four transport equations for k_p, ε_p, k_t, and ε_t; the governing equations for these quantities can be found in [7, 13]. In the Nichols-Nelson multi-scale approach, Menter's SST RANS model, which itself is a blend of the k-ω and k-ε models (see section 2.2.3) is employed as the near wall model; the k-ω model operates at the very near-wall and transitions to the k-ε model, which, in the Nichols-Nelson formulation, is modeling the large scale turbulence, k_p and ε_p. The large-scale turbulent parameters found from the k_p-ε_p transport equations are then filtered to be implemented into the LES subgrid model, which is a nonlinear k-equation model.

The turbulent length scale that is incorporated into the filter function is determined with the unfiltered RANS turbulence model values (indicated with RANS subscript):

$$L_T = \max\left(6.0\sqrt{\frac{\nu_{T_{RANS}}}{\Omega}}, \frac{k_{RANS}^{\frac{3}{2}}}{\varepsilon_{RANS}}\right), \tag{2.36}$$

where $\nu_{T_{RANS}}$ is the standard SST model eddy viscosity, k_{RANS} and ε_{RANS} are attained via the k_p-ε_p transport equations, that is $k_{RANS} = k_{p,unf\ iltered}$ and $\varepsilon_{RANS} = \varepsilon_{p,unf\ ilterea}$. The subgrid turbulent kinetic energy is defined as

$$k_{LES} = k_{RANS} f_d, \tag{2.37}$$

where the filter function is

$$f_d = \frac{1 + \tanh\left[2\pi\left(\Lambda - 0.5\right)\right]}{2} \tag{2.38}$$

where

$$\Lambda = \frac{1.0}{1.0 + \left(\frac{L_T}{L_G}\right)^{\frac{4}{3}}} \tag{2.39}$$

The grid length scale can be defined as it is in Eqn. (2.33), or, as another effort to smooth the transition, it can be defined as

$$L_G = \left(\Delta x \Delta y \Delta z\right)^{\frac{1}{3}} \tag{2.40}$$

The LES-based subgrid kinematic turbulent viscosity is

$$\nu_{T_{LES}} = \min\left(.0854 L_G \sqrt{k_{LES}}; \nu_{T_{RANS}}\right), \tag{2.41}$$

and the composite kinematic turbulent viscosity is calculated via

$$\nu_T = \nu_{T_{RANS}} f_d + \left(1 - f_d\right)\nu_{T_{LES}}. \tag{2.42}$$

In addition to differing from SA-DES in incorporating the turbulent length scale into the filter function, the Nichols-Nelson hybrid method calculates the turbulent viscosity based on the subgrid kinetic energy, a quantity that is absent in the Smagorinsky model (equation 2.31) used in conjunction with DES. It is noted, though, the Nichols and Nelson , take the subgrid turbulent kinetic energy as the filtered RANS turbulent kinetic energy rather than using a k transport equation, which would incorporate more physical processes, such as the convection, productions, and dissipation of subgrid kinetic energy.

CHAPTER THREE

Flow Simulation

Six cases with various Reynolds and Mach numbers (see Table 1.1) are presented in this study. Deck's ZDES case [4] was used as a basis for fluid flow generation. The first two cases aimed to reproduce ZDES fluid flow results from [4], one case using Spalart-Allmaras DES (1-SA-DES) and the other Nichols-Nelson hybrid RANS/LES (1-NN), by using similar computational domain dimensions and grid spacing, inlet boundary layer thickness $\delta_0 = 3.56$ mm, and Reynolds number based on inlet boundary layer thickness, $Re_{\delta 0}$; the free-stream parameters for these two cases are as follows: Mach number is $M = 0.5$ with velocity $U_\infty = 170$ m/sec, static pressure is $P = 41.4$ kPa, and static temperature is $T = 287$ K. (See Table 1.1). For the next two cases, again one using SA-DES (2-SA-DES) and one using Nichols-Nelson hybrid RANS/LES (2-NN), to show dependence on Re_θ, the inlet boundary layer thickness was increased to $\delta_0 = 6.39$ mm (and the computational domain dimensions increased by the same ratio) to induce a Re_θ increase without changing the free-stream velocity. Finally, to show dependence on Mach number, the last two cases (3-SA-DES and 3-NN) retain the higher δ_0 (and associated computational domain dimensions) and free-stream parameters, except the

Mach number which is increased to $M = 0.9$ with velocity $U_\infty = 1003$ m/sec. Both hybrid models have been implemented into the WIND-US 3.0 code [30] for generating flow fields used in the present study.

Table 3.1. Description of cases studied.

Case	Model	Mach Number	δ_0 [mm]	$Re_{\delta 0}$	Re_θ
1-SA-DES	Spalart-Allmaras DES	0.5	3.56	17000	4159
1-NN	Nichols-Nelson hybrid	0.5	3.56	17000	3018
2-SA-DES	Spalart-Allmaras DES	0.5	6.39	29000	7704
2-NN	Nichols-Nelson hybrid	0.5	6.39	29000	8235
3-SA-DES	Spalart-Allmaras DES	0.9	6.39	52000	18180
3-NN	Nichols-Nelson hybrid	0.9	6.39	52000	19430

3.1 Boundary Conditions

The accuracy of flow computation and the convergence properties of the solution are heavily dependent upon boundary conditions. Wind-US 3.0 uses a cell-vertex discretization to compute the boundary values (the solution at points located on the boundaries of the zones that comprise the flow domain) for the conservative and turbulence variables. [30]. By default, the boundary conditions are imposed explicitly each iteration, after the interior solution has been computed for each zone; the zone interfaces, though, are updated each time level [30]. In the current study, implicit boundary conditions are used for the wall-boundary to improve stability. The boundary conditions remain consistent throughout all six cases.

inflow: Turbulent inflow data is generated with the pseudo-turbulent routine described in Section 1.2 (4) in a box consisting of 64x64x64 points that bounds the inflow boundary

y-z plane and matches the plate's spanwise dimension and extends to the initial boundary layer thickness in the wall-normal direction. To generate inlet flow turbulence, the "box" of frozen turbulence is computed, and these perturbations are fed into the inlet every time step and subsequently carried by the mean flow into the computational domain. The first step in the turbulence computation process is to calculate a pseudorandom divergence-free isotropic velocity field that conforms to a prescribed energy spectrum. This field is computed within the cubic domain using default values for peak energy wave number (8.0), based on box-size, and random seed number (987.0). Within the specified inflow boundary layer height, the turbulence is scaled accounting for the boundary layer. It is computed on a uniform Cartesian grid.

outflow: Specifying an outflow boundary condition for downstream outflow boundaries is recommended for external flow; in the current study, a constant exit pressure is specified. This option can result in reflective behavior, thus it is applied to outflow of the sponge layer designed to prohibit pollution of the region of interest.

viscous wall: The viscous wall boundary condition imposes a no-slip condition of the flow, a zero pressure gradient, and the adiabatic heat transfer condition at the wall surface [30]. To minimize the transients at the start of a Wind-US 3.0 calculation, the velocity at no-slip boundaries is reduced from its initial value to the no-slip condition over 50 iterations by default [30], though for the present simulation that value is set to 1.

reflective side walls: The reflection boundary condition simulates a plane of symmetry and is the same as a solid, inviscid wall boundary condition which imposes flow tangency at the zone boundary while maintaining the same total velocity as the point adjacent to the boundary [30].

3.2 Spatial and Temporal Schemes

A third order HLLC (Harten-Lax-van Leer for Contact) [25] upwind-biased solver is employed for calculation of the first derivative (non-viscous) terms on the right-hand side of Wind's equation set; the left-hand side of Wind's equation set is computed with an implicit point Jacobi operator, for which 10 sub-iterations are allowed per time step. Time marching is governed by a second order implicit scheme that incorporates 3 global Newton iterations per time step.

3.3 Calculation Domain

For all cases, no-slip and adiabatic boundary conditions are imposed at the bottom wall, the top boundary and outflow boundaries are free-stream, and the sides are symmetric.

3.3.1 Case 1

The computational domain extends $78\delta_0$, $10\delta_0$, and $5\delta_0$ in the streamwise, wall-normal, and spanwise directions, respectively, and is comprised of a Cartesian mesh, uniform in the streamwise and spanwise directions and stretched wall normal direction in the near-wall region (up to $y^+ \approx 100$), but uniform in the remainder of the domain to accommodate LES modeling. The grid spacing in viscous wall units are $\Delta x^+ \approx 125$, $\Delta z^+ \approx 50$, $\Delta y^+_{min} \approx 1.7$ based on downstream conditions. A $24\delta_0$ sponge layer is applied to the outlet boundary to ensure that the outflow condition does not pollute the region of

interest. The grid consists of 396, 128, and 61 grid points in the streamwise, wall-normal, and spanwise directions, respectively, for a total of 3,091,968 grid points.

3.3.2 Cases 2 and 3

The computational domain extends $75\delta_0$, $10\delta_0$, and $3\delta_0$ in the streamwise, wall-normal, and spanwise directions, respectively, and is comprised of a Cartesian mesh, uniform in the streamwise and spanwise directions and stretched wall normal direction in the near-wall region (up to $y^+ \approx 100$), but uniform in the remainder of the domain. The grid spacing in viscous wall units are $\Delta x^+ \approx 160$, $\Delta z^+ \approx 64$, $\Delta y^+_{min} \approx 1.8$ based on downstream conditions. A $13\delta_0$ sponge layer is applied to the outlet boundary. The grid consists of 657, 214, and 61 grid points in the streamwise, wall-normal, and spanwise directions, respectively, for a total of 8,576,478 grid points.

3.4 Temporal Considerations

For all cases, data collection for statistics was taken after a minimum of three flow-through-times and taken over a minimum period of one flow-through-time. The details for each case are presented in Table 2 below.

Table 3.2. Beginning and length of time period over which statistics were calculated for each case studied, given in terms of the normalized time step and flow-through-times.

	Time Step	Beginning of Collection Period		Length of Collection Period	
Case	$[\delta_0/U_\infty]$	$[\delta_0/U_\infty]$	flow-through-times	$[\delta_0/U_\infty]$	flow-through-times
1-SA-DES	$1.52\text{x}10^{-2}$	400	5.10	123	1.57
1-NN	$1.52\text{x}10^{-2}$	400	5.10	108	1.37
2-SA-DES	$8.51\text{x}10^{-3}$	349	4.64	128	1.70
2-NN	$8.51\text{x}10^{-3}$	255	3.40	85.1	1.13
3-SA-DES	$1.53\text{x}10^{-2}$	230	3.05	76.5	1.02
3-NN	$1.53\text{x}10^{-2}$	230	3.05	76.5	1.02

3.5 Methodology

To fully utilize the capability of hybrid LES/RANS turbulence model and avoid long calculation domain associated with spatially developing boundary layer flows [4], a prescribed lower section of the domain is setup to model a developing boundary layer; this allows for an initial boundary thickness, δ_0, to form at the point of contact between the prescribed layer and the free stream that will grow to a desired thickness; this is the mixing layer method mentioned in section 1.2 (5). The initial boundary layer thickness is designed to be 10 percent of the inlet calculation domain (δ_0 = 3.56 mm for the case 1 set, δ_0 = 6.39 mm for the case 2 and 3 sets). The Reynolds number based on initial boundary layer thickness is $Re_{\delta 0}$ = 17000, $Re_{\delta 0}$ = 29000, and $Re_{\delta 0}$ = 52000 for case sets 1, 2, and 3, respectively.

3.6 Data Output

For each case, a job was initiated and allowed to run for several flow-through times (see section 3.3) prior to collecting data for statistical calculations; periodically, an intermediate flow field data file was created, as well as a file including the time history of specified variables: u, v, and w velocity, density, temperature, turbulent viscosity and laminar viscosity along specified vertical lines of sight. The intermediate flow field data files were converted to PLOT3D format and visualized in ParaView to monitor the results qualitatively. The time history file was interpreted with the Wind-US 3.0 *thplt* utility to check for statistical convergence. Since only data along a vertical line of sight can be saved to the time history file, for the period of time during which data was collected for statistical analysis, a flow field data file was saved every time step; each was

converted to a geometrically truncated PLOT3D format file, and processed with ParaView. The geometric truncation reduces the disk space required for the files by only retaining a portion of the computational domain, cutting out the first $27\delta_0$ from the leading edge of the plate and the sponge region. Within ParaView, the interpolated variable values were computed along a specified line of sight using the scheme described on the following page:

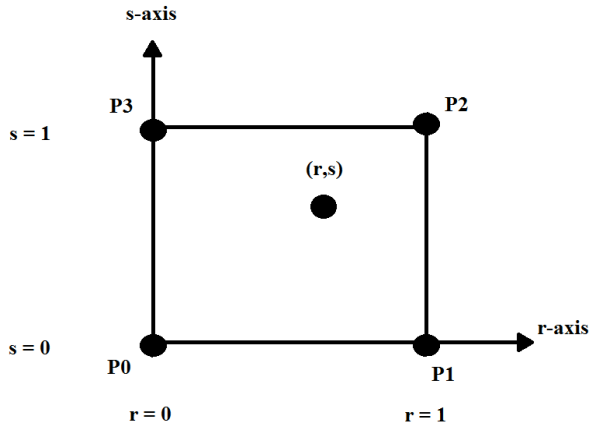

Figure 3.1. Representation of interpolation scheme used for lines of sight at elevation angles other than 90 degrees.

The weighting, w_i, is such that

$$w_0 = (1-r)(1-s) \tag{3.1}$$

$$w_1 = r(1-s) \tag{3.2}$$

$$w_2 = rs \tag{3.3}$$

$$w_3 = (1-r)s \tag{3.4}$$

where r and s are the coordinates of the interpolation point. The interpolated value, d is calculated by

$$d = \sum w_i d_i \tag{3.5}$$

where d_i is the data value at point P_i. For example, if $r = s = 0.5$ (i.e., the point is centrally located) then the interpolated value is

$$d = .25d_0 + .25d_1 + .25d_2 + .25d_3 \tag{3.6}$$

It should be noted that the above scheme is a relatively simple one compared to those used in other published aero-optic papers.

CHAPTER FOUR

Results and Discussion

4.1 Spatial Development

The turbulent boundary layer that forms on a flat plat continually develops, so the statistics are dependent upon both x and y. To produce statistically relevant profiles to compare with those found in the literature, it is necessary to perform statistical calculations along a line of sight that originates from a streamwise station within a region of fully developed flow. Figure 4.1 on the following page shows instantaneous realizations of the evolving velocity field on a truncated domain (see section 3.6). Because the flow is unsteady, one cannot determine spatial development qualitatively by examining these instantaneous realizations of the velocity field. Instead, statistical calculations must be performed along at least a few downstream locations.

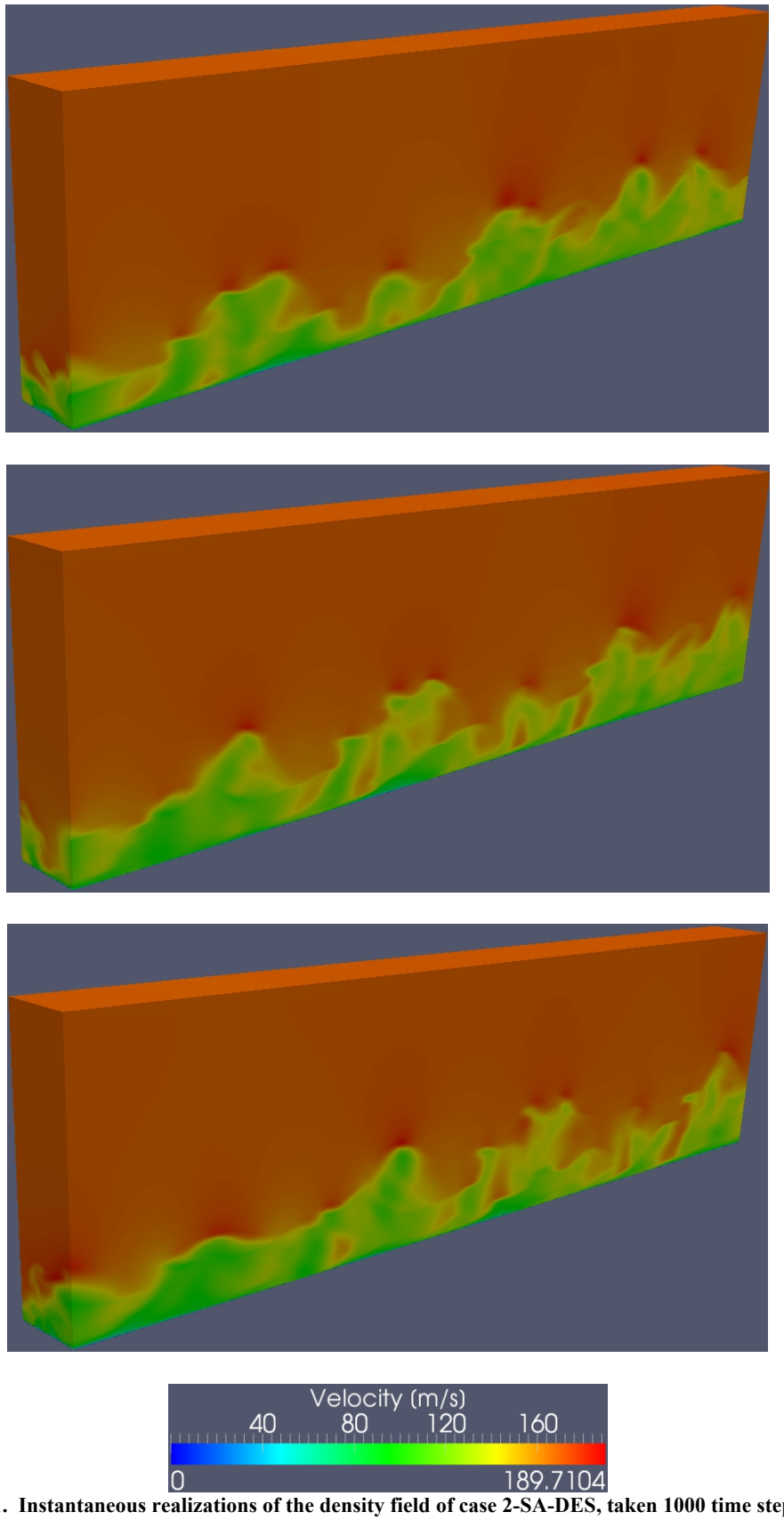

Figure 4.1. Instantaneous realizations of the density field of case 2-SA-DES, taken 1000 time steps apart.

To choose a streamwise station for the vertical direction along which the statistics are taken, spatial development is considered for each set of cases by plotting the r.m.s. velocity fluctuations at three streamwise stations. Figure 4.2 on the following page shows the r.m.s. velocity fluctuations at $66\delta_0$, $68\delta_0$, and$70\ \delta_0$ for the Case 1 set, indicating that the flow is fully developed at $68\delta_0$; hence, this is the streamwise station used for the Case 1 set statistics.

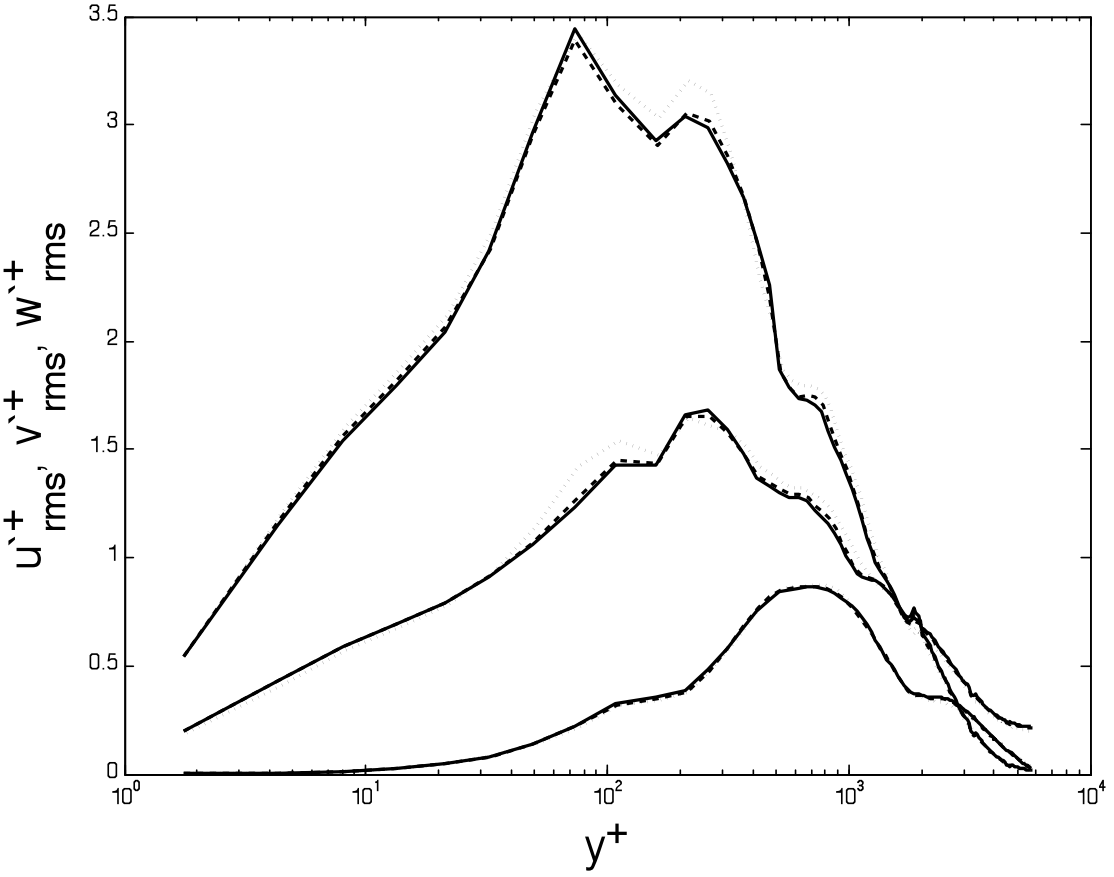

Figure 4.2. Velocity component fluctuation r.m.s. at streamwise station $66\delta_0$ (dotted), $68\delta_0$ (dashed), $70\delta_0$ (solid).

Similarly, the streamwise stations for the Case 2 set and Case 3 were both appropriately chosen to be at $70\ \delta_0$.

4.2 Validation with Experimental Data

To validate the aero-dynamical fields, this section presents statistical profiles of velocity and density along a line of sight originating from a streamwise station in the fully developed region and extending in the wall-normal direction. Figure 4.3(a) shows the mean velocity profile normalized by wall parameters (friction velocity, wall distance, kinematic viscosity) in Van Driest form for case 1-SA-DES, and Figure 4.3(b) is for case 1-NN. For Case 1-SA-DES, good comparisons within viscous sub-layer, logarithmic and outer regions are obtained and agree with experimental data obtained using hot-wire velocimetry by [12] (see [26]); however, the Nichols-Nelson hybrid model fails to produce an adequate mean velocity profile. For the mean density profile normalized by the free-stream density shown in Figure 4.4(a) and 4.4(b), the agreement between the current hybrid results and the LES results of [29] is satisfactory for both cases; these LES results are for an adiabatic Mach 0.4 case, so the difference in Mach number could account for the small discrepancy at the inlet for Case 1-NN.

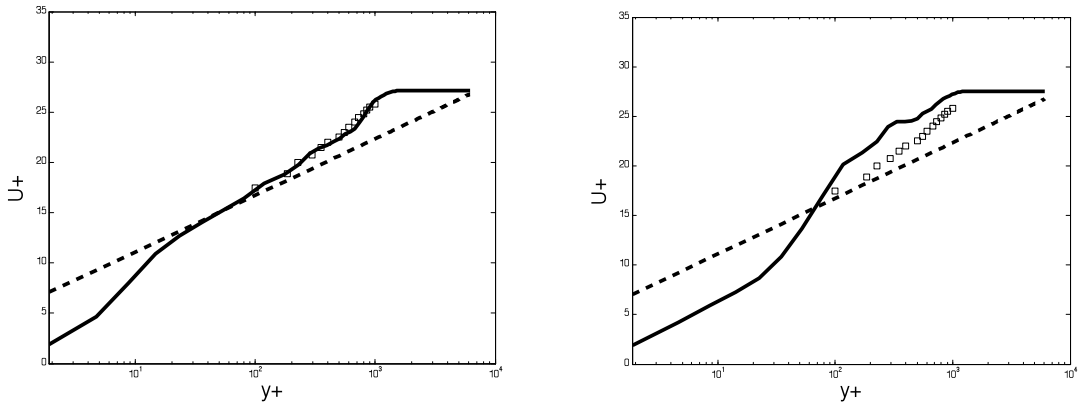

(a) **(b)**

Figure 4.3. Mean field velocity profiles for case 1-SA-DES (a) and 1-NN (b): velocity (solid line), experimental data (squares), $U^+ = 2.44 \ln y^+ + 5.2$ (dashed line)

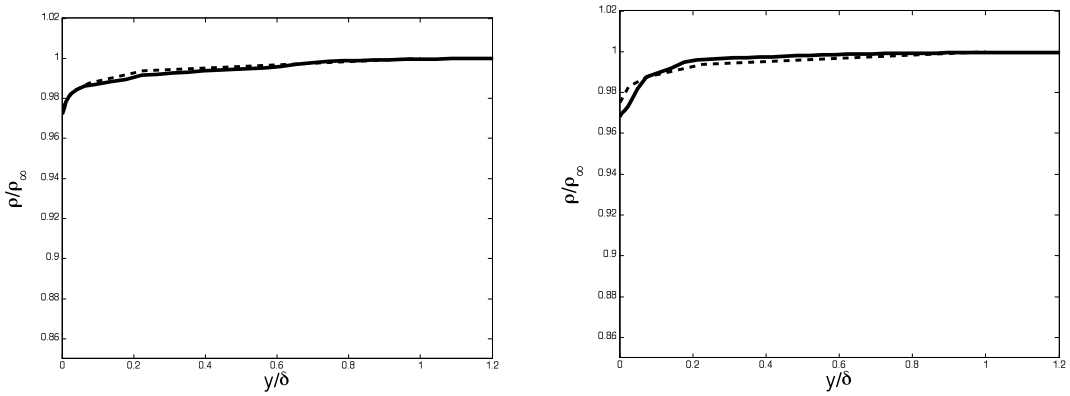

(a) **(b)**

Figure 4.4. Mean field density profiles for case 1-SA-DES (a) and 1-NN (b): density (solid line), LES results (dashed line)

In the following, fluctuating density field is shown. Figure 4.5(a) and 4.5(b) show the profile along the direction normal to the plate and is compared with scaled experimental data from a Mach 0.89 case [12] (cited in [29]). The scaling method of [29] is employed. The measurement uncertainty of the experimental data is cited as around 10 percent by [26]; the level of discrepancy between the magnitude of the modeled density fluctuation for Case 1-NN and that of the experimental data is encountered with LES modeling in both [26] and [29]. The peak location for Case 1-NN is similar to that of said LES cases in terms of the boundary layer thickness, 0.1δ and 0.05δ, respectively. Physically, though, the location of the peak shown by 1-NN is at the higher end of the logarithmic layer, while [27] shows peaks at the lower end of the logarithmic layer. Despite these differences, the Nichols-Nelson hybrid approach is a better candidate for fluctuating density field prediction than SA-DES, as the modeled density fluctuation for Case 1-SA-DES is too low in the near wall region to be considered acceptable.

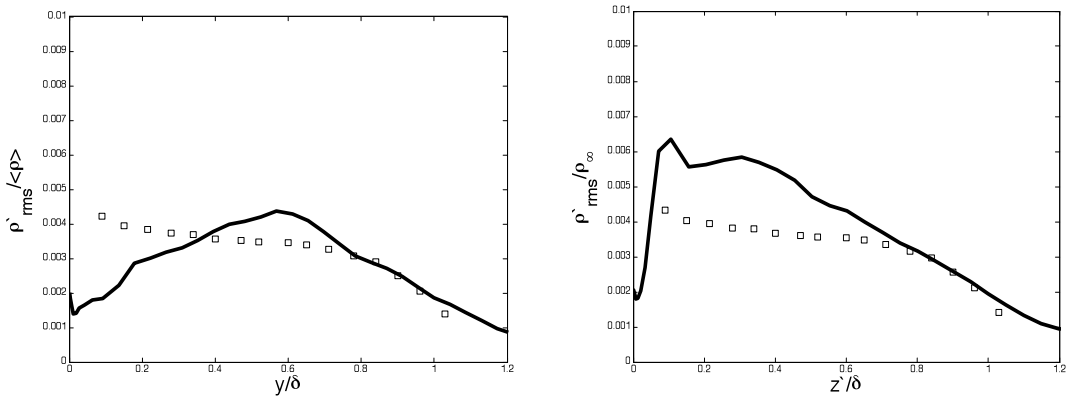

(a) **(b)**

Figure 4.5. Profile of r.m.s. density fluctuations along a wall-normal view vector, normalized by the free-stream density, for case 1-SA-DES (a) and 1-NN (b): r.m.s. density fluctuations (solid line), experimental data (squares)

Spalart-Allmaras DES better predicts mean flow velocity statistics, while density fluctuation results using Nichols-Nelson hybrid are superior and closely resemble those produced by LES. The fluctuating streamwise velocity component also shows the Nichols-Nelson results more closely resembling those of LES than does SA-DES. In figure 4.6, the streamwise velocity fluctuation along a vertical line is shown along with laser-Doppler anemometer experimental data for $Re_\theta = 2900$ from [5].

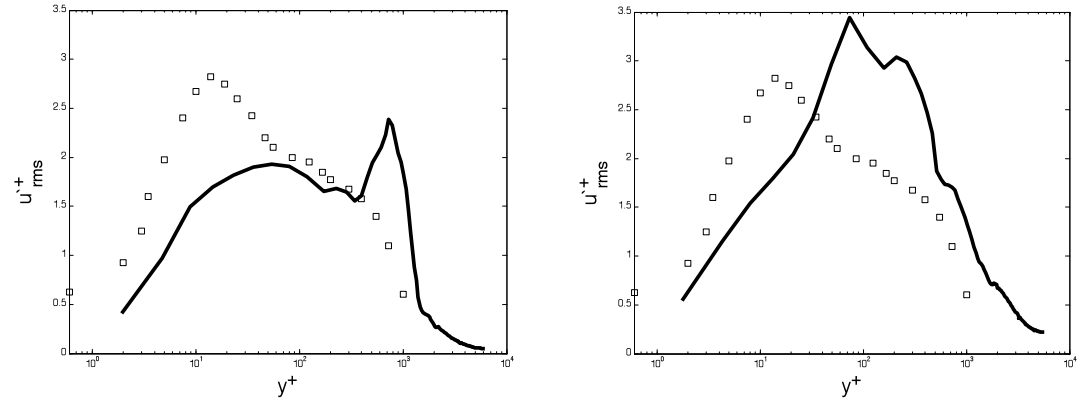

(a) **(b)**

Figure 4.6. Profile of r.m.s. streamwise veloctiy fluctuations a wall-normal view vector, normalized by the free-stream density at β = 90 degrees, for case 1-SA-DES (a) and 1-NN (b): r.m.s. velocity fluctuations (solid line), experimental data (squares)

The level of discrepancy between the peak value of the Nichols-Nelson modeled velocity fluctuation and that of the experimental data (20 percent) is nearly matched by the LES results reported by Deck (15 percent) [4]. The peak displacement, also noted in the density fluctuation in Figure 4.4(b), indicates a possible inner layer modeling problem. Nevertheless, the results of case 1-NN better match the shape of the curve than those of SA-DES, which again yields low, smooth near-wall fluctuation peak and a secondary peak in the outer region of the boundary layer that is inconsistent with profiles found in the literature.

The notable difference between the two models is the turbulent viscosity, shown with the normalized mean velocity profile in Figure 4.7.

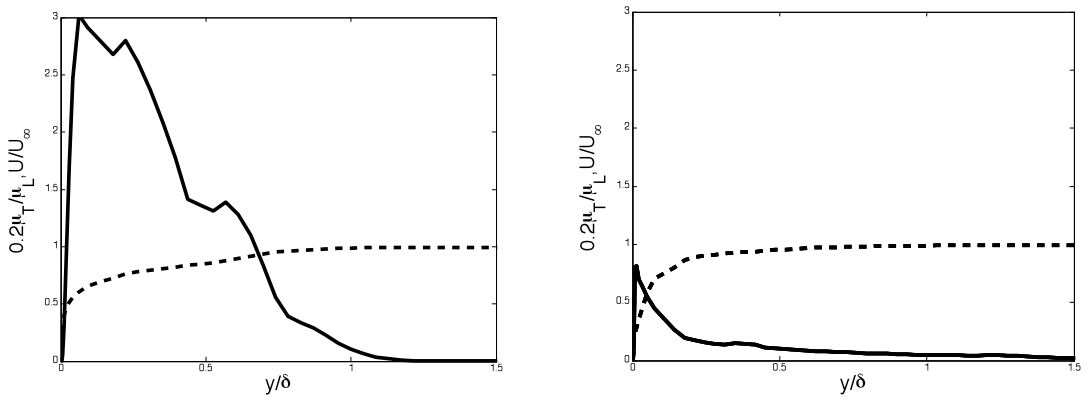

(a) **(b)**

Figure 4.7. Turbulent viscosity profiles for case 1-SA-DES (a) and 1-NN (b): $0.2\mu_T/\mu_L$ (solid line), mean velocity normalized with the free-stream velocity (dashed line)

SA-DES yields a much higher peak value of turbulent viscosity, and maintains a higher turbulent viscosity throughout the boundary layer; this indicates that SA-DES retains a RANS solution further in the wall-normal direction than the Nichols-Nelson model; RANS inherently fails to capture unsteady motions, thus it follows that the fluctuation would be damped in the RANS region of a hybrid RANS/LES model, as

shown in Figures 4.5(a) and 4.6(a). Another way to illustrate the extended RANS region in SA-DES is observing the velocity fluctuation at three different wall-normal stations, as in Figure 4.8 below.

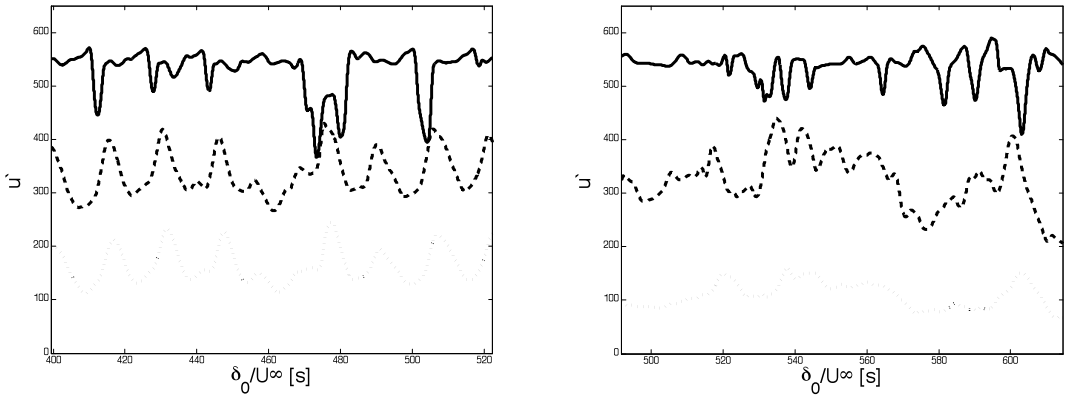

(a) **(b)**

Figure 4.8. Instantaneous velocity for case 1-SA-DES (a) and 1-NN (b) at $y^+ = 8$ (dotted), $y^+ = 80$ (dashed), $y^+ = 954$ (solid)

The instantaneous velocity exhibits periodic behavior for the SA-DES case (a); the low-frequency fluctuations observed associated with RANS models [16] are apparent for the SA-DES, but not for the NN-hybrid. Farther away from the wall, at a y^+ location of nearly 1000, both models show the higher frequency fluctuations associated with LES.

The RANS retention associated with SA-DES explains the difference in the skin friction coefficient, shown in Figure 4.9. The data point included, from DeGraaff and Eaton [5], is the skin friction coefficient for fully developed flow; they give a table of skin friction values for several values of Re_θ.

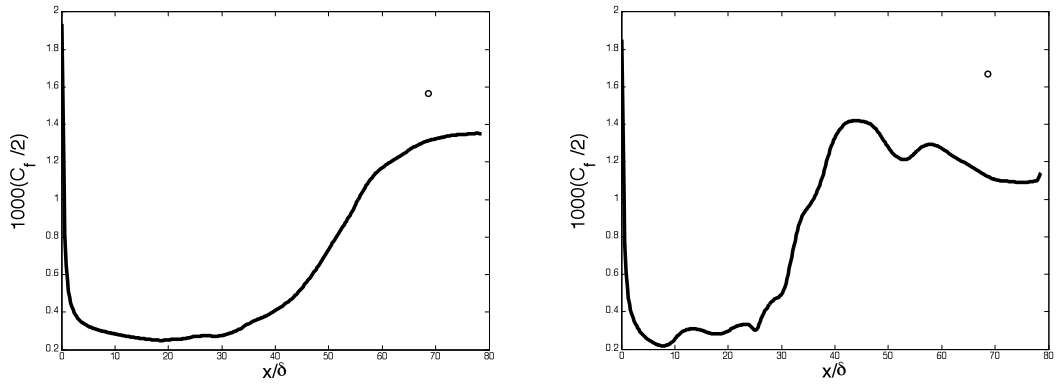

(b) **(b)**

Figure 4.9. Skin friction coefficient for case 1-SA-DES (a) and 1-NN (b): experimental data (circle)

The skin friction coefficient profile is much smoother for SA-DES than for Nichols-Nelson hybrid RANS/LES; again, the RANS portion of SA-DES could be contributing to a more consistent near-wall velocity, producing a more consistent skin friction coefficient.

Since the fluctuating density field is of primary concern for aero-optics, the remainder of the results shown will be illustrating elevation angle dependence of density fluctuations for Case 1-NN, showing the mean velocity profile and density fluctuation dependence on Re_θ and then on Mach number. The density field data will be taken from the Nichols-Nelson cases, and velocity profiles from the Spalart-Allmaras cases.

4.3 Dependence on Elevation Angle

It is well established that the turbulent boundary layer has packets of vortical structures with a preferred angular direction oriented downstream. Thus, aero-optic aberrations also exhibit an anisotropic behavior for various oblique angles. This effect was shown as the downstream-direction propagation through the elongated structures that resulted in more area under the density fluctuation profile, directly proportional to aberration, versus propagation in the upstream direction. Figure 4.10 shows the root

mean square values of the density fluctuation profile across the boundary layer along the chief ray at different elevation angles β. The angle is defined such that 0^o is the upstream direction, 90^o is the wall-normal direction and 180^o is the downstream direction. The optical grid coordinate, z' , describes the optical path in the direction of propagation (i.e, it is identical to the wall-normal-coordinate for flow for the case in which the optical path extends normal to the plate). While figure 4.5(b) shows the profile along the chief ray normal to the plate (β = 90 degrees), Figures 4.10(a) and 4.10(b) show the profiles along a chief ray at angles of 60 degrees and 120 degrees, respectively.

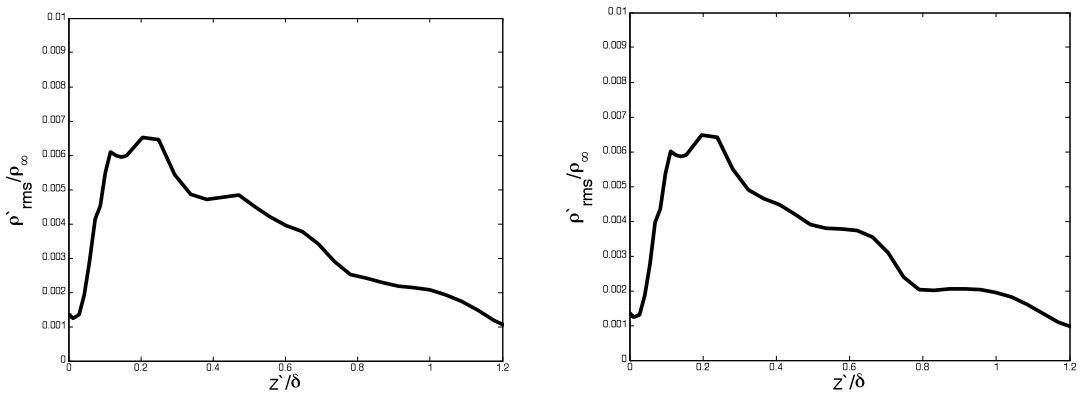

(a) **(b)**

Figure 4.10. Profile of r.m.s. density fluctuations, normalized by the free-stream density along a view vector elevated to (a) β =60 degrees, (b) 120 degrees

The difference between Figure 4.10(a) and 4.10(b) is difficult to detect; to make the trend more apparent, the two-point density correlation for a reference point at 0.30δ, at the three elevation angles, is presented in Figure 4.11.

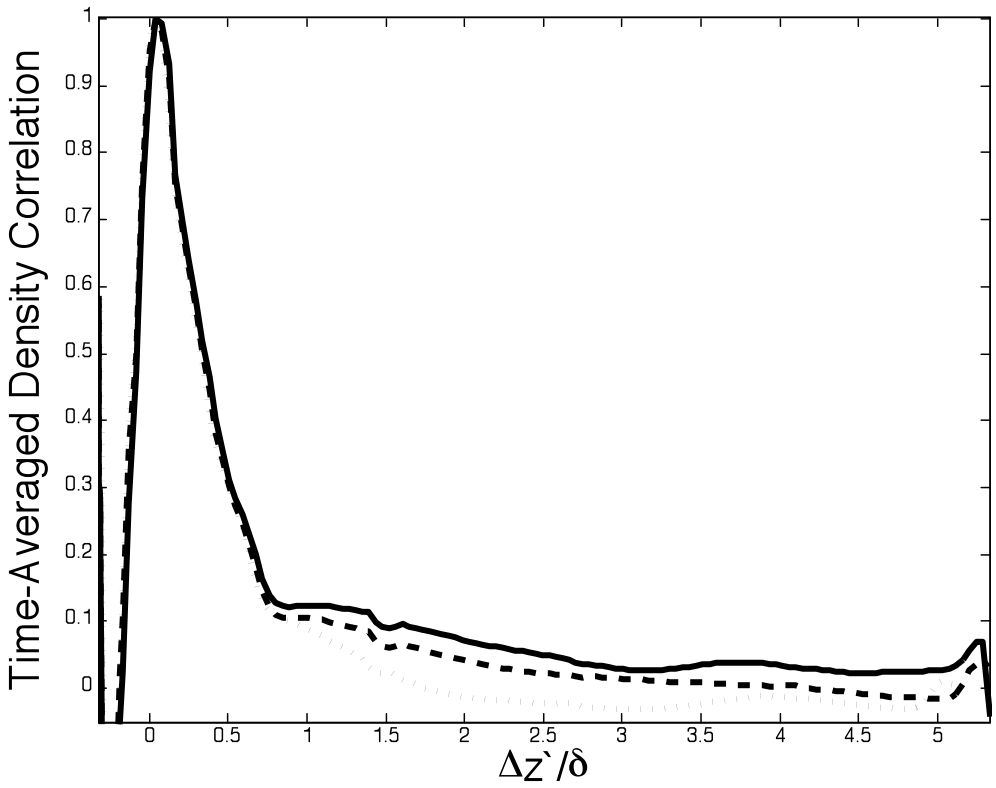

Figure 4.11. Two-point correlation of density fluctuations, normalized by the free-stream density, along a view vector elevated to β = 60 degrees (dotted), 90 degrees (dashed), 120 degrees (solid); the reference point is 0.30δ, where δ is local boundary layer thickness.

As evident in Figure 4.11, at the two angles β = 60 degrees and β = 120 degrees, which are symmetric relative to the wall-normal direction, the correlation functions differ such that the correlation lengths (integration of the correlation function) at 120 degrees are larger than those at 60 degrees. This observation supports the downstream orientation of the vertical structures and shows that the optical distortions are more severe for the beam tilted toward the downstream direction than that toward the upstream, even if they travel the same distance [28].

The increasing trend of the correlation length with increasing distance of the reference point from the wall is noted by Figure 4.12 which shows the two-point density correlation for β = 90 degrees at three different reference points.

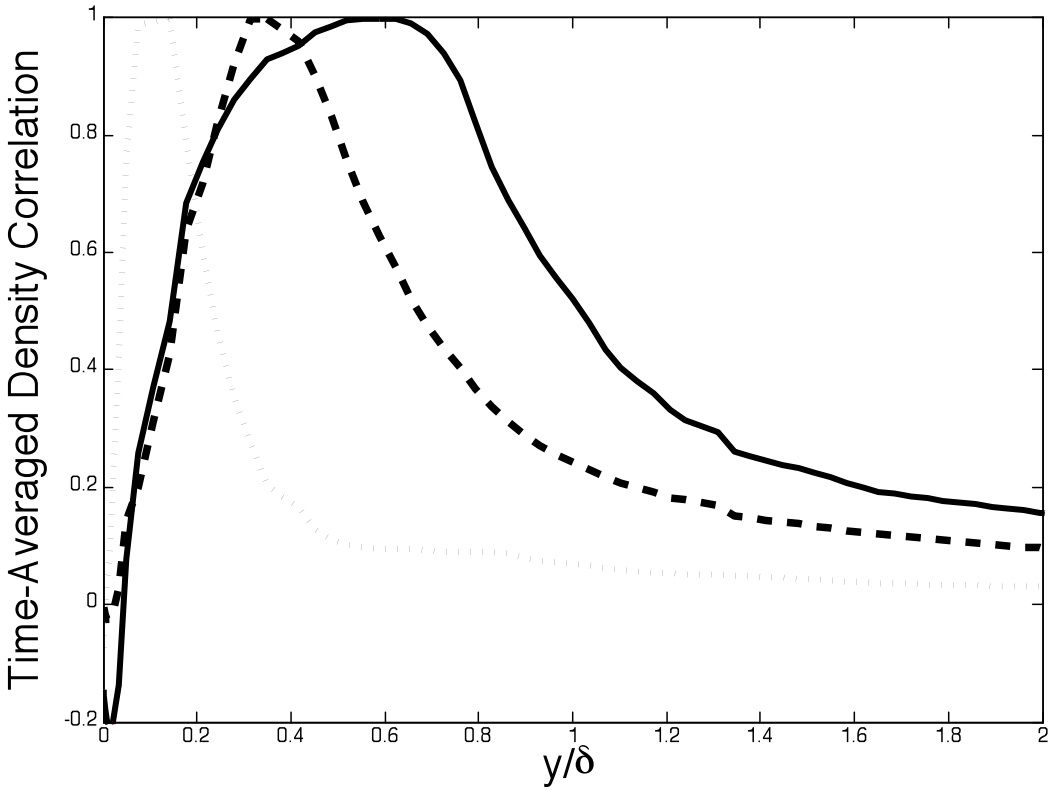

Figure 4.12. Time-averaged two-point density correlation, y/δ (normalized distance from the wall) = .10 (dotted); y/δ= .40 (dashed); y/δ= .70 (solid); δ is local boundary layer thickness

Finally, one can observe tilted vortical structure phenomena in instantaneous realizations of the density flow field, shown in Figure 4.13 on the following page.

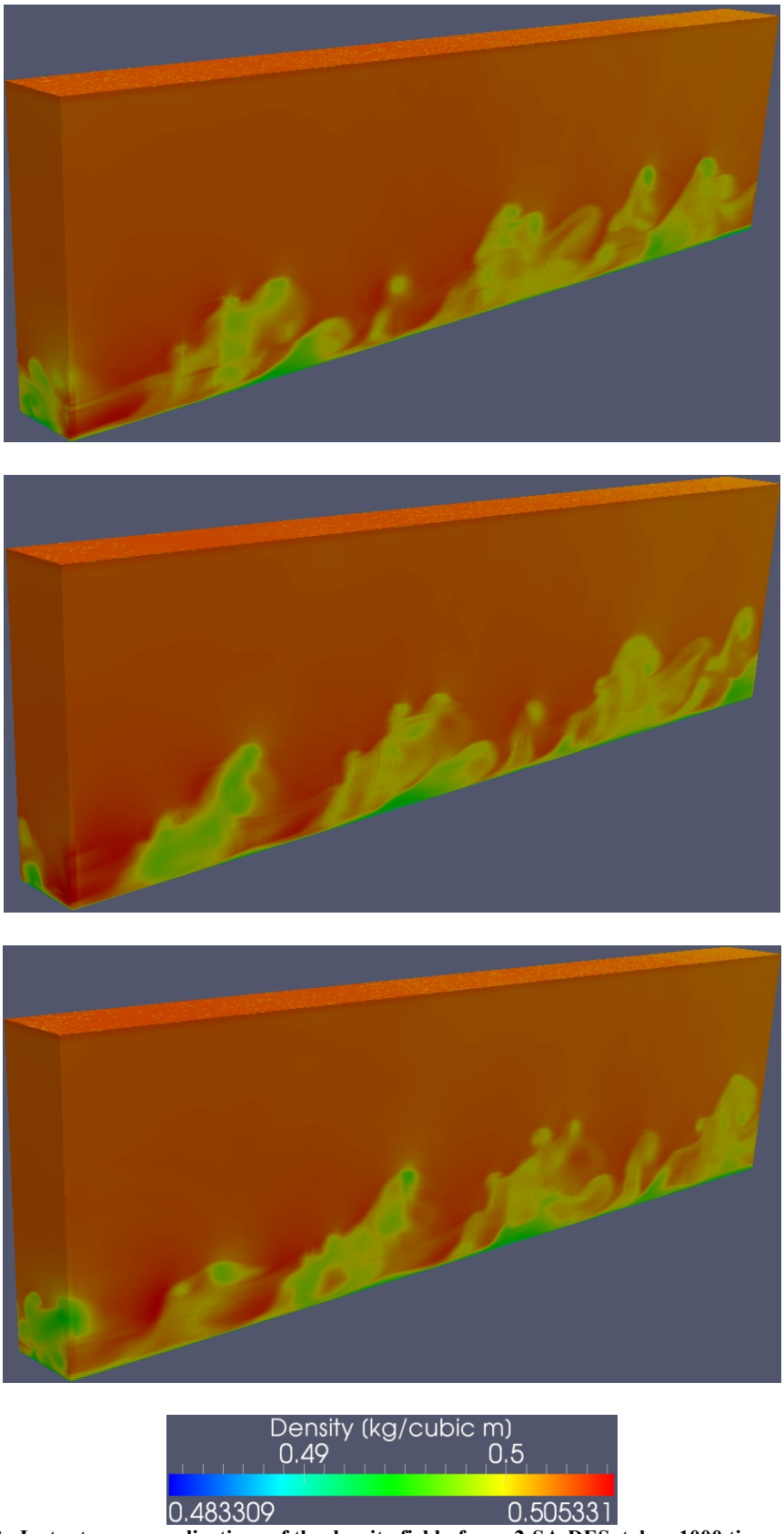

Figure 4.13. Instantaneous realizations of the density field of case 2-SA-DES, taken 1000 time steps apart.

4.4 Dependence on Re_θ and Mach Number

In this section, Re_θ and Mach number dependence are illustrated for profiles along vertical lines of sight ($\beta = 90$ degrees). To show dependence on Re_θ, the velocity profile of 1-SA-DES and the r.m.s. density fluctuation profile of 1-NN are compared to those of 2-SA-DES (Figure 4.14) and 2-NN (4.15), respectively. Recall that case 1 and 2 have the same Mach number, but differ in initial boundary layer thickness, and thus Re_θ.

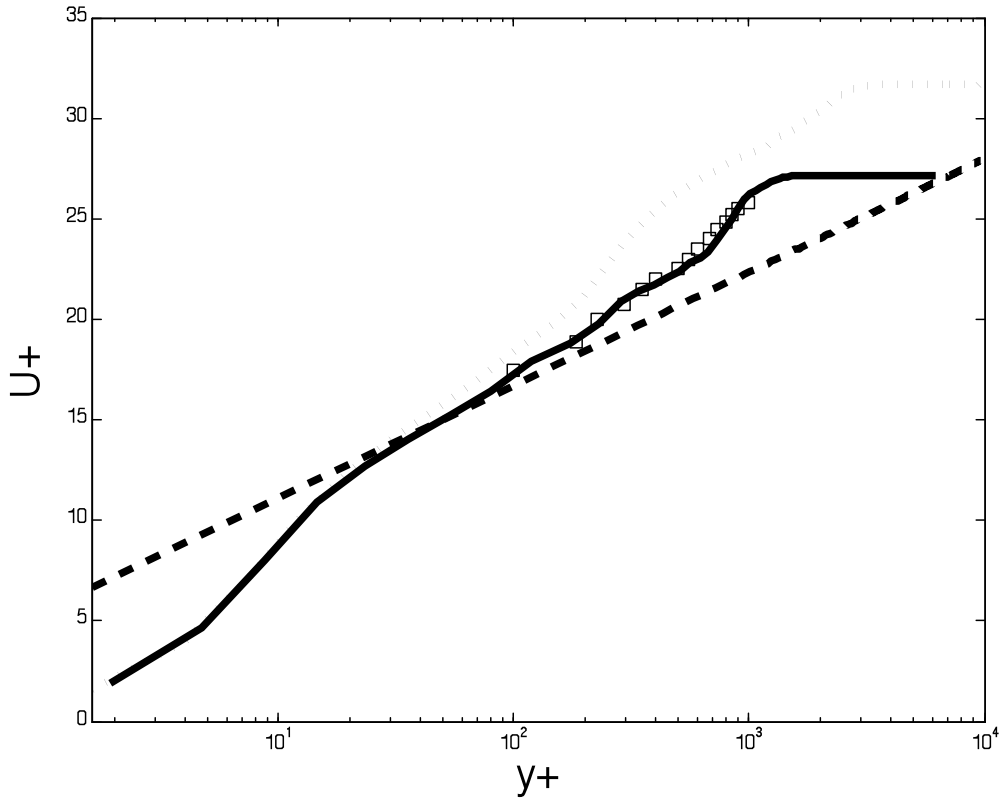

Figure 4.14. Mean field velocity profiles for case 1-SA-DES, Re_θ = 4159 (solid) and 2-SA-DES Re_θ = 7704 (dotted), experimental data (squares), $U^+ = 2.44 \ln y^+ + 5.2$ (dashed).

Figure 4.14 above illustrates an increase in the mean velocity at the edge of the boundary layer (where the profiles level off) with an increase in Re_θ. This is the expected trend, also observed by [27]. The discrepancy between the modeled mean velocity and

the experimental values in the outer region is noted; however, the modeled velocity still exhibits satisfactory alignment with the slope in the logarithmic region.

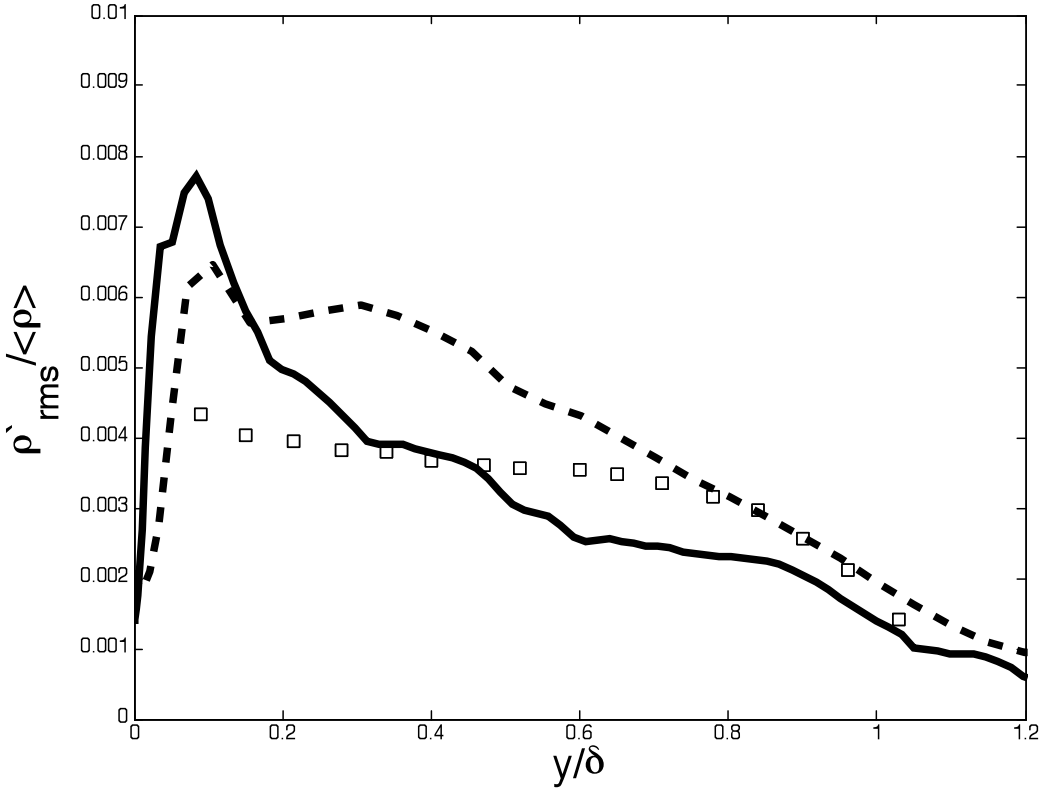

Figure 4.15. Profile of r.m.s. density fluctuations for case 1-NN, $Re_\theta = 3018$ (dashed) and 2-NN $Re_\theta = 8235$ (solid), experimental data (squares).

In Figure 4.15, the peak of the density fluctuation is higher for the higher Re_θ, however, the total area under the curve is smaller, which would yield a lower correlation length; this trend is supported by the findings of [27].

To show dependence on Mach number, the velocity profile of 2-SA-DES and the r.m.s. density fluctuation profile of 2-NN are compared to those of 3-SA-DES (Figure 4.16) and 3-NN (4.17), respectively. Recall that case 2 and 3 have the same boundary layer thickness, but differ in Mach number.

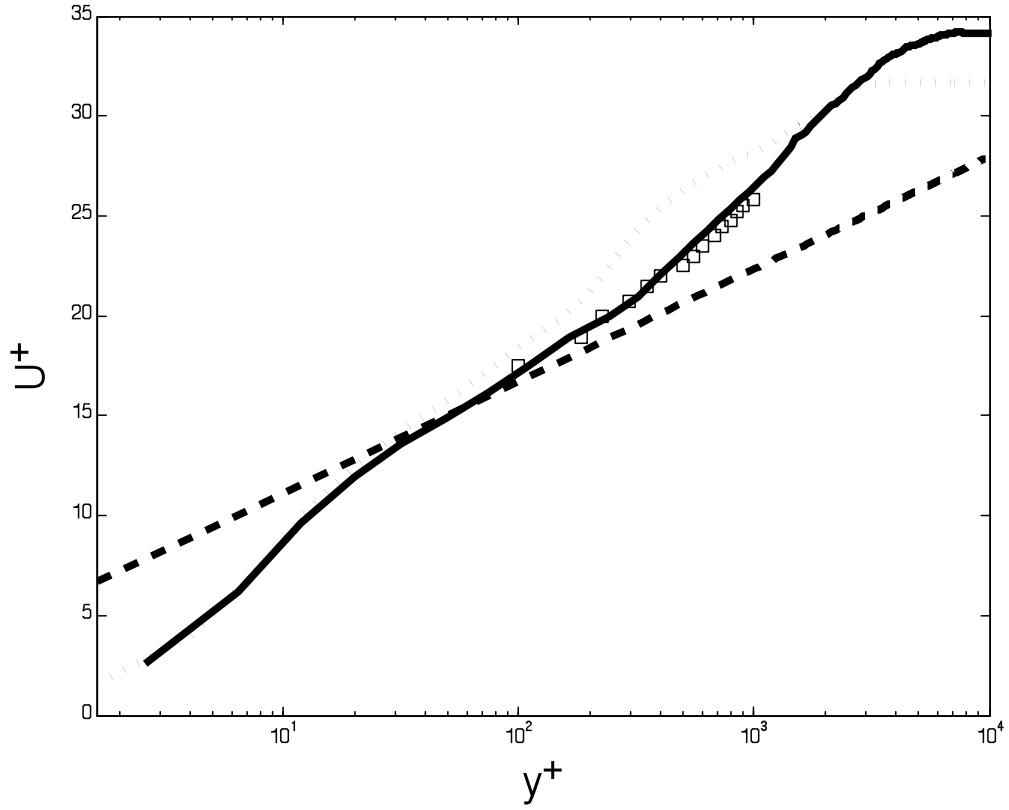

Figure 4.16. Mean field velocity profiles for case 2-SA-DES, Re_θ = 7704, *M* = 0.5 (dotted) and 3-SA-DES Re_θ =18180, *M* = 0.9 (solid), experimental data (squares), $U^+ = 2.44 \ln y^+ + 5.2$ (dashed).

Figure 4.16 illustrates a further increase in the mean velocity at the edge of the boundary layer with an increase in Mach number; however, since the Re_θ also drastically increases, further information is required for Figure 4.16 to conclusively indicate a dependence on Mach number. The momentum thickness increases two-fold from case 1-SA-DES to 2-SA-DES and only by 25 percent from case 2-SA-DES to 3-SA-DES; with this information, one can conclude that the increase in the mean velocity at the edge of the boundary layer is mostly due to the increase in Mach number, as the higher velocity the main contributor to the increase in Re_θ.

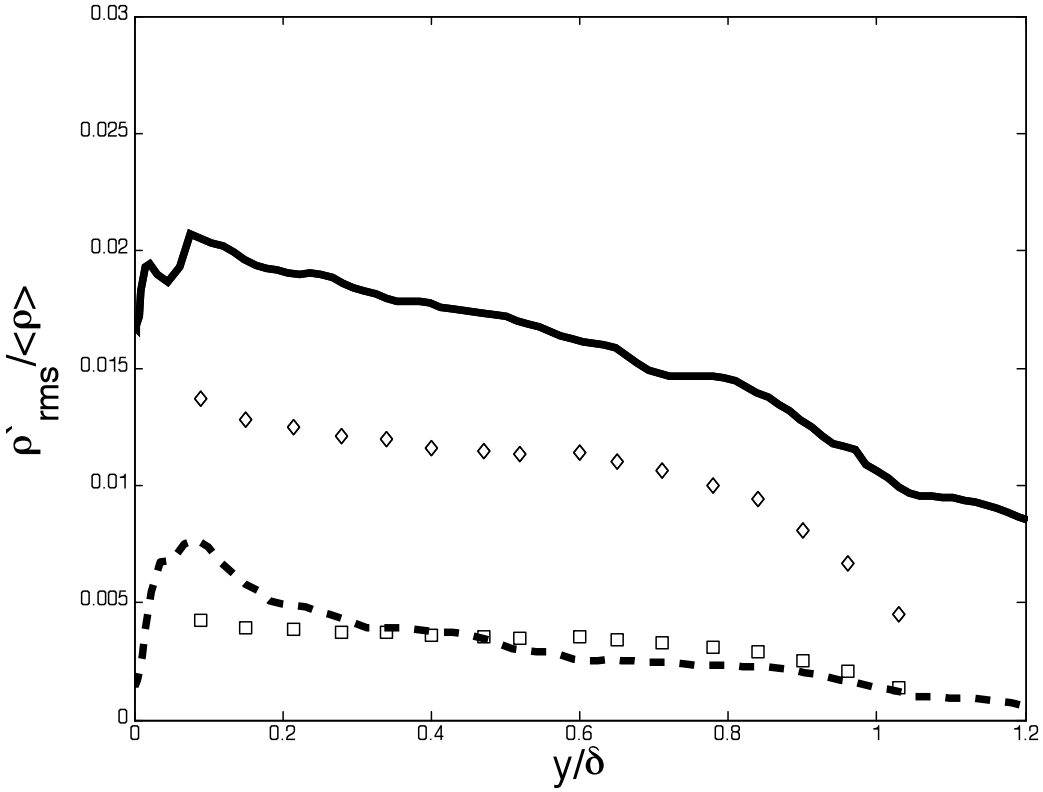

Figure 4.17. Profile of r.m.s. density fluctuations for case 2-NN, $Re_\theta = 8235$, $M = 0.5$ (dashed) and 3-NN $Re_\theta = 19430$, $M = 0.9$ (solid), experimental data (squares).

In Figure 4.17, the peak and total area under the curve of the density fluctuation is higher for the higher Mach number; since a decrease is expected with an increase in Re_θ, the increase in total area under the curve can be attributed solely to the increased Mach number. The stronger effect of the Mach number than Re_θ is also noted in [27].

CHAPTER FIVE

Conclusions and Recommendations

The formulation and results of two hybrid RANS/LES models have been presented in this work; the following conclusions can be made:

(1) The cases using Spalart-Allmaras Detached Eddy Simulation showed accurate predictions of mean flow variables. In all SA-DES cases the mean velocity profiles adhered to the law of the wall. In cases 1-SA-DES and 3-SA-DES, the outer layer velocity profile showed excellent agreement with experimental data.

(2) Comparative analysis of the SA-DES cases showed an increase in the mean velocity at the edge of the boundary layer with an increase in Re_θ, and the same observation is made for an increase in Mach number.

(3) Nichols-Nelson hybrid RANS/LES model adequately predicts the density fluctuation within the flow. Interest in aero-optic effects, for which the fluctuating density field is most significant, motivated moving forward with the Nichols-Nelson model.

(4) Dependence of density fluctuation on elevation angle was illustrated with r.m.s. density fluctuation profiles and two-point density correlations for lines of sight elevated to 60, 90, and 120 degrees, ultimately predicting more severe optical distortions for a beam that is tilted toward the downstream direction, than for one aiming toward the

upstream; this conclusion is intuitive given that the vortical structures in turbulent flow are oriented toward the downstream.

(5) As a basis for creating a scaling law, the density fluctuation profiles were compared for two flows with different Re_θ , $Re_\theta \approx 3000$ and $Re_\theta \approx 8000$, and then for two flows with different Mach numbers, $M = 0.5$ and $M = 0.9$. It is predicted that the optical distortion will decrease with increasing Re_θ, and increase with increasing Mach number.

(6) Finally, a proposed solution to the slowly developing boundary layer (described in section 3.5) was confirmed as a relatively low-cost method of adequately representing flow with an initial boundary layer thickness; this is a contribution to flat plate boundary layer flow simulation in general as finding an alternative to naturally developing boundary layer growth is a universal challenge.

While the flow field quantity of most interest, the density fluctuation, was modeled to an adequate degree of accuracy, the cases presented did not show satisfactory results for all flow aspects. In the cases studied, Spalart-Allmaras Detached Eddy Simulation accurately predicted mean flow variables, but under-predicted the fluctuation near the wall, while the Nichols-Nelson hybrid RANS/LES model adequately predicted the fluctuation within the flow, but failed to yield a mean velocity profile that follows the law of the wall; the flow is very much dependent on inlet conditions and grid resolution, neither of which were necessarily optimized for this study, thus several recommendations are offered. The most severe problems with the models occur in the inner region of the boundary layer, where the behavior of the model near the wall, the turbulent inflow condition (applied only within the boundary layer), boundary layer development, and near-wall grid spacing all play a crucial role.

(1) The most significant difference between the two models is apparent in their predictions of the turbulent viscosity; SA-DES retains a RANS solution much farther in the wall-normal direction than does the Nichols-Nelson hybrid model. Since the modeling the turbulent viscosity seems to be the crux of boundary layer problem, perhaps an alteration in the Nichols-Nelson switching (blending) function could render the model more useful for the flat plate case.

(2) Employing a higher-fidelity method, such as a precursor simulation with flow recycling, could lead to a more realistic prediction of the turbulent motion within the boundary layer.

(3) The approach used in the current study to increase the inlet boundary layer thickness would be vastly improved if a velocity profile could be prescribed at the inlet; this option is currently being investigated for incorporation into the Wind-US 3.0 code; another option would be the use of a wall-function, which would force a log-law and also reduce computational cost.

(4) The grid for the current cases was generated based on that of a successful Zonal-Detached Eddy Simulation case [4]; ideally, a grid refinement study would have been performed and more trouble-shooting with respect to the near-wall grid spacing would have been done. Additionally, extension of the computational domain in the streamwise direction to incur a longer fully developed region is not necessary but would provide confidence that some of the issues are not associated with flow that is not fully developed.

(5) In the interest of high-fidelity aero-optic results for different view angles, a more higher-order interpolation scheme is suggested.

The flow fields generated in and the information provided by this study is useful to the aero-optical applications [2x4] as it demonstrates the methodology's capability of supplying accurate anisotropic aero thermal fields due to anisotropic non-homogeneous turbulent flows.

REFERENCES

[1]Basu, Debashis, "Hybrid Methodologies for Multiscale Separated Turbulent Flow Simulations," Ph.D. thesis, University of Cincinnati, 2006.

[2]Baurle, R. A., Tam, C.-J., Edwards, J. R., and Hassan, H. A., "Hybrid Simulation Approach for Cavity Flows: Blending, Algorithm, and Boundary Treatment Issues," AIAA paper 2001-2562, 2001.

[3]Davidson, L. and Billson, M., "Hybrid LES-RANS using synthesized turbulent fluctuations for forcing in the interface region," *Int. J. Heat and Fluid Flow,* Vol. 27, 1028–1042, 2006.

[4]Deck, S., Weiss, P.-E., Pamiès, M. and Garnier, E., "Zonal detached eddy simulation of a spatially developing flat plate turbulent boundary layer," *Computers and Fluids*, Vol. 48, 1-15, 2011.

[5]DeGraaff, D. B. and Eaton, J. K. "Reynolds-number scaling of the flat-plate turbulent boundary layer," *J. Fluid Mech.,* Vol. 422, 319-346, 2000.

[6]Garnier, E., Adams, N., Sagaut, P. "Large Eddy Simulation for Compressible Flows," Springer, 2009.

[7]Kim, S. W. and Chen, C. P., "A Multiple-Time-Scale turbulence model based on variable partitioning of the turbulent kinetic energy spectrum," *Numerical Heat Transfer, Part B: Fundamentals*, Vol. 16, 193-212, 1989.

[8]Lee, S., Lele, S. K. and Moin, P., "Simulation of spatially evolving turbulence and the applicability of Taylor's hypothesis in compressible flows," *Physics of Fluids A*., Vol. 4, 1521-1530, 1992.

[9]Lund T., Wu X., Squires, K. "Generation of turbulent inflow data for spatially developing boundary layer simulations," *J. Comput. Phys.,* Vol. 140, 233–258, 1998.

[10]Menter, F. R. and Rumsey, C. L., "Assessment of two-equation models for transonic flows," AIAA paper 94-2343, 1994.

[11]Moin, P. and Mahesh, K. "Direct numerical simulation: A tool in turbulence research," *Annu. Rev. Fluidmech.,* Vol. 30*,* 539-578, 1998.

[12]Mucini S, Breil J. F., Mignosi A and Dussauge J P., Echelles de turbulence en couche limite transsonique *Rapport de l'Institut Universitaire des Systémes Thermiques Industriels* Marseille, 2001.

[13]Nichols, R. H. and Nelson, C. C., "Application of Hybrid RANS/LES Turbulence Models," AIAA paper 2003-0083, 2003.

[14]Nichols, R. H., "Comparison of Hybrid Turbulence Models for a Circular Cylinder and a Cavity," *AIAA Journal,* Vol. 44, 1207-1219, 2006.

[15]Patil, S. and Tafti, D. "Wall modeled large eddy simulations of complex high Reynolds number flows with synthetic inlet turbulence." *Intl. J. of Heat and Fluid Flow*, Vol. 33, 9-21, 2012.

[16]Piomelli, U., "Large-eddy simulation: achievements and challenges", *Progress in Aerospace Sciences*, Vol. 35, 173-197, 1999.

[17]Pope, S. B. "Turbulent flow." Cambridge University Press, New York, 2000.

[18]Rutland, C. J. "Large-eddy simulations for internal combustion engines – a review," *International Journal of Engine Research*, Vol. 12, 421-451, 2011.

[19]Shang, J. S., "Three decades of accomplishments in computational fluid dynamics", *Progress in Aerospace Sciences*, Vol. 40, 173-197, 2004.

[20]Sillero, J. et al "Direct simulation of a zero-pressure-gradient turbulent boundary layer up to $Re_\theta = 6650$," J. Physics: Conf. Series 318, 2011.

[21]Spalart P. R. and Allmaras S. R. "A one equation turbulence model for aerodynamic flows," AIAA paper 1992-0439, 1992.

[22]Spalart, P. R., "Detached-Eddy Simulation," *Annu. Rev. Fluid Mech.,* Vol. 41, 181-201, 2009.

[23]Strelets, M., "Detached Eddy Simulation of Massively Separated Flows," AIAA Paper 2001-0879, Jan. 2001.

[24]Sutton, G.W., "Aero-Optical Foundations and Applications," *AIAA Journal,* Oct. 1525-1537, 1985.

[25]Toro, Eleuterio F., *Reimann Solvers and Numerical Methods for Fluid Dynamics*, Springer-Verlag, New York, 2009. (3rd Edition, pages 314-344)

[26]Tromeur, E., Garnier, E. and Sagaut, P., "Analysis of the Sutton model for aero-optical properties of compressible boundary layers," *J. Fluids Eng.,* Vol. 128, 239-246, 2006.

[27]Wang, K. and Wang, M., "Aero-optical distortions by subsonic turbulent boundary layers," AIAA paper 2011-3278, 2011.

[28]Wang K, Wang M. "Numerical simulation of aero-optical distortions by a turbulent boundary layer and separated shear layer," AIAA paper 2009-4223, 2009.

[29]White, M. D. and Visbal, M. R., "High fidelity analysis of aero-optical interaction with compressible boundary layer," AIAA paper 2010-4496, 2010.

[30]WIND US 3.0 user's guide, NPARC alliance, (http://www.grc.nasa.gov/WWW/wind/index.html), 2011.